Impact of stratospheric air and surface emissions on tropospheric nitrous oxide during ATom

Yenny Gonzalez[1,2,3], Róisín Commane[1,4], Ethan Manninen[1], Bruce C. Daube[1], Luke Schiferl[4], J. Barry McManus[5], Kathryn McKain[6,7], Eric J. Hintsa[6,7], James W. Elkins[6], Stephen A. Montzka[6], Colm Sweeney[6], Fred Moore[6,7], Jose L. Jimenez[7], Pedro Campuzano Jost[7], Thomas B. Ryerson[8], Ilann Bourgeois[7,8], Jeff Peischl[7,8], Chelsea R. Thompson[8], Eric Ray[7,8], Paul O. Wennberg[9,10], John Crounse[9], Michelle Kim[9], Hannah M. Allen[10], Paul Newman[11], Britton B. Stephens[12], Eric C. Apel[13], Rebecca S. Hornbrook[13], Benjamin A. Nault[14], Eric Morgan[15] and Steven C. Wofsy[1]

[1] John A. Paulson School of Engineering and Applied Sciences, Harvard University, Cambridge, MA 02138, USA
[2] CIMEL Electronique, Paris, 75011, France
[3] Izaña Atmospheric Research Centre, Santa Cruz de Tenerife, 38001, Spain.
[4] Dept. of Earth and Environmental Science, Lamont-Doherty Earth Observatory, Columbia University, New York, NY 10964, USA
[5] Center for Atmospheric and Environmental Chemistry, Aerodyne Research Inc., Billerica, MA 01821, USA
[6] NOAA Global Monitoring Laboratory, Boulder, CO 80305, USA.
[7] Cooperative Institute for Research in Environmental Sciences, CIRES, University of Colorado Boulder, Boulder, CO 80309, USA.
[8] NOAA Chemical Sciences Laboratory, Boulder, CO 80305, USA.
[9] Division of Geological and Planetary Sciences, California Institute of Technology, Pasadena, CA 91125, USA.
[10] Division of Chemistry and Chemical Engineering, California Institute of Technology, Pasadena, CA, 91125, USA
[11] NASA Goddard Space Flight Center, Greenbelt, MD 20771, USA.
[12] Earth Observing Laboratory, National Center for Atmospheric Research (NCAR), Boulder, CO 80301, USA.
[13] Atmospheric Chemistry Observations & Modeling Lab, NCAR, Boulder, CO 80301, USA.
[14] Center for Aerosol and Cloud Chemistry, Aerodyne Research, Inc., Billerica, MA, 01821, USA
[15] Scripps Institution of Oceanography, University of California San Diego, CA 92037, USA.

Correspondence to: Róisín Commane (r.commane@columbia.edu)

Abstract. Nitrous oxide (N_2O) is both a greenhouse gas in the troposphere and an ozone depleting substance in the stratosphere and is rapidly increasing in the atmosphere. The spatial distribution of N_2O emissions and the sources leading to rising mixing ratios in the global atmosphere are highly uncertain. We measured the global distribution of tropospheric N_2O mixing ratios during the airborne Atmospheric Tomography (ATom) mission. ATom measured mixing ratios of ~300 gas species and aerosol properties in 647 vertical profiles spanning the Pacific, Atlantic, Arctic, and much of the Southern Ocean basins, from nearly Pole to Pole, over four seasons (2016–2018). We measured N_2O mixing ratios at 1 Hz using a Quantum Cascade Laser Spectrometer and a new spectral retrieval method to account for

the pressure and temperature sensitivity of the instrument when deployed on aircraft. This retrieval strategy improved the precision of our N_2O measurements by a factor of 3, enabling us to recover the precision to that of previous missions. Most of the variance of N_2O mixing ratios in the troposphere is driven by the influence of N_2O-depleted stratospheric air, especially at mid and high latitudes. We observe the downward propagation of lower N_2O mixing ratios (compared to surface stations) that tracks the influence of stratosphere-troposphere exchange through the tropospheric column down to the surface, resulting in a seasonal minimum at the surface 2–3 months after the peak stratosphere-to-troposphere exchange in spring. The highest N_2O mixing ratios occur close to the equator, extending through the boundary layer and free troposphere. We observed influences from a complex and diverse mixture of N_2O sources, with emission source types identified using the rich suite of chemical species measured on ATom and with the geographical origin calculated using an atmospheric transport model. Although ATom flights were mostly over the oceans, the most prominent N_2O enhancements were associated with anthropogenic emissions, including industry, oil and gas, urban and biomass burning, especially in the tropical Atlantic outflow from Africa. Enhanced N_2O mixing ratios are mostly associated with pollution-related tracers arriving from the coastal area of Nigeria. Peaks of N_2O are often well-correlated with indicators of photochemical processing, suggesting possible unexpected source processes. The difficulty of separating the mixture of different sources in the atmosphere contributes to uncertainties in the N_2O global budget. The extensive data set from ATom will help improve the understanding of N_2O emission processes and their representation in global models.

1. Introduction

Nitrous oxide (N_2O) is a powerful greenhouse gas and a major contributor to both stratospheric ozone loss and to passivation of stratospheric oxy-halogen radicals (Forster et al., 2007; Ravishankara et al., 2009). The increasing rate of 0.93 nmol mol^{-1} yr^{-1} of atmospheric N_2O since the industrial revolution implies significant (~30%) imbalance between emission rates and destruction in the stratosphere. Seasonal cycles in tropospheric N_2O are driven by both stratosphere-to-troposphere exchange and by surface emissions (Nevison et al., 2011; Assonov et al., 2013; Thompson et al., 2014a). Most N_2O emissions are attributed to microbial nitrification and denitrification in natural and cultivated soils, freshwaters and oceans, plus emissions related to human activities such as fertilization, biomass burning and industry (Butterbach-Bahl et al., 2013; Saikawa et al., 2014; Thompson et al., 2014a; Upstill-Goddard et al., 2017; WMO, 2018).

Much effort has been made to reduce the uncertainties in the individual components of the N_2O global budget (e.g., Tian et al., 2012, 2020; Xiang et al., 2013; Thompson et al., 2014a, b; Ganesan et al., 2020; Yang et al., 2020). Recent estimates of global total N_2O emission to the atmosphere from bottom-up and top-down methods average 17 Tg N yr^{-1} (12.2–23.5 from bottom-up analysis, and 15.9–17.7 Tg N yr^{-1} from top-down approaches, Tian et al., 2020). The magnitude of marine N_2O emissions is subject to large uncertainty, due to spatial and temporal heterogeneity (Nevison et al., 1995, 2005; Ganesan et al., 2020; Yang et al., 2020). The most recent estimates of the global ocean emission of

80   N$_2$O range between 2.5 and 4.3 Tg N yr^{-1}, with the tropics, upwelling coastal areas and subpolar regions the major contributors to these fluxes (Yang et al., 2020; Tian et al., 2020). Agricultural N$_2$O emission estimates range between 2.5 and 5.8 Tg N yr^{-1}, and between 4.9 and 6.5 Tg N yr^{-1} in the case of natural soils (Kort et al., 2008; 2010; Syakila and Kroeze, 2011; Tian et al., 2020). Recent estimates of N$_2$O emissions from fertilized tropical and subtropical agricultural systems are 3 ± 5 kg N ha^{-1} y^{-1} (Albanito et al., 2017). N$_2$O emissions from tropical river systems in Africa

85   are estimated at 3.3 ± 1.3 Tg N$_2$O yr^{-1} (Valentini et al., 2014). According to Tian et al. (2020), anthropogenic sources account for 43% of the global N$_2$O emissions (7.3 Tg N yr^{-1}), with industry and biomass burning emissions estimated to be 1.6 to 1.9 Tg N yr^{-1} respectively (Syakila and Kroeze, 2011; Tian et al., 2020) and the balance from agriculture. Most of these estimates are derived from short-term local-scale in-situ measurements and are difficult to extrapolate with confidence to large regions or to the globe.

90   In the atmosphere, N$_2$O is destroyed by oxidation and photolysis in the upper stratosphere, which makes it a good candidate for tracing the air exchange between the stratosphere and the troposphere (Hintsa et al., 1998; Nevison et al., 2011; Assonov et al., 2013; Krause et al., 2018). Atmospheric models tend to underestimate the inter-hemispheric N$_2$O gradient, which Thompson et al. (2014a) attribute to an overestimation of N$_2$O emissions in the Southern Ocean, an underestimate of the Northern Hemisphere emissions, and/or an overestimate of stratosphere-to-troposphere exchange

95   in the Northern Hemisphere. Overall, the largest uncertainties of modelled N$_2$O emissions are found in tropical South America and South Asia (Thompson et al., 2014b).

We present highly resolved atmospheric N$_2$O profiles collected during the NASA Atmospheric Tomography (ATom) mission. ATom was a global scale airborne deployment conducted over a 3-year period (2016–2018) using the NASA DC-8 aircraft. In ATom, the DC-8 flew vertical profiles (0.2–13 km) nearly continuously while measuring

100   mixing ratios of ~300 trace gases and aerosol physical and chemical properties over the Pacific and Atlantic basins from nearly Pole to Pole and during each of the four seasons. Each deployment started and ended in Palmdale (California, USA). Each deployment ($1 - 4$) generally consisted of a loop southward from the Arctic through the central Pacific, across the Southern Ocean to South America, northward through the Atlantic, and across Greenland and the Arctic Ocean. During ATom-3 and -4, two additional flights from Punta Arenas (Chile) sampled the Antarctic

105   troposphere and Upper Troposphere/Lower Stratosphere (UT/LS) to 80° S.

In this work we focus on the measurements taken during January–February 2017 (ATom-2), September–October 2017 (ATom-3), and April - May 2018 (ATom-4) (no QCLS N$_2$O data are available for ATom-1 in Aug.). The motivation for this paper is twofold. Firstly, we present a new retrieval strategy to account for the pressure and temperature dependence of laser-based instruments, specifically for the use of quantum cascade laser spectrometers on

110   aircraft. Secondly, we report on the global distribution of N$_2$O from the surface to 13 km, and examine the processes contributing to the variability of tropospheric N$_2$O based on the vertical profiles of N$_2$O and a broad variety of co-variate chemical species and aerosol properties.

2 Instrument specifications, spectral analysis and calibration

115 ### 2.1 Specifications of the QCLS

We measured N_2O mixing ratios with the Harvard/NCAR/Aerodyne Research Inc. Quantum Cascade Laser Spectrometer (QCLS). This instrument was previously deployed on the NCAR/NSF Gulfstream V for the HIAPER Pole-to-Pole Observations mission (HIPPO, Wofsy et al., 2011; https://www.eol.ucar.edu/field_projects/hippo) and the O_2/N_2 Ratio and CO_2 Southern Ocean Study (ORCAS, Stephens et al., 2018;

120 https://www.eol.ucar.edu/field_projects/orcas). Detailed information about the spectrometer configuration can be found in Jiménez et al. (2005, 2006) and Santoni et al. (2014). A brief description follows.

QCLS provides continuous (1 Hz) and highly spectrally resolved measurements of N_2O, methane (CH_4) and carbon monoxide (CO) using two thermoelectrically-cooled pulsed quantum cascade lasers, a 76 m pathlength multiple pass absorption cell (~ 0.5 L volume), and two liquid-nitrogen cooled solid-state HgCdTe detectors. All these components

125 are mounted on a temperature-stabilized, vibrationally isolated optical bench. The temperature in QCLS is controlled by Peltier elements coupled with a closed-circuit recirculating fluid kept at 288.0 ± 0.1 K. QCLS measures CH_4 and N_2O by scanning the spectral interval of 1275.45 ± 0.15 cm^{-1}. A second laser is used to scan CO at 2169.15 ± 0.15 cm^{-1}. The supply currents to QCLS are ramped at a rate of 3.8 kHz to scan the laser frequency for 200 channels (steps in frequency) in laser 1 and 50 channels in laser 2, with an extra 10 channels to measure the laser shut off (zero-light

130 level). The spectra and fit residual for CH_4, N_2O and CO are shown in Fig. S1 of the Supplement. Mixing ratios are derived at a rate of 1 Hz by a least-squares spectral fit assuming a Voigt line profile at the pressure and temperature measured inside the sample cell and using molecular line parameters from the HIgh-resolution TRANsmission molecular absorption database (HITRAN, Rothman et al., 2005). The temperature and pressure inside the cell are monitored with a 30 kΩ thermistor and a capacitance manometer (100 Torr full scale).

135 During sampling, the air passes through a 50-tube Nafion drier to remove the bulk water vapor. A Teflon diaphragm pump downstream of the cell reduces the air pressure to ~60 mbar. Both ambient air and calibration gases pass through a Teflon dry-ice trap to reduce the dew point to –70 °C. After ATom-1, we added a bypass between the inlet and the instrument to increase the flushing rate of the inlet and inlet tubing. The calibration sequence includes 2 minutes of Ultra-High Purity zero air, followed by 1 minute each of low- and high-mixing ratio gases every 30 minutes (see Fig.

140 S2). During ATom-1 and -2, we measured zero air every 15 minutes, and every 30 minutes during ATom-3 and -4. A data logger (CR10X, Campbell Scientific) was used to automate the sampling sequence. The CR10X also regulated pressure and temperature and managed the data transfer.

We use gas cylinders traceable to the National Oceanic and Atmospheric Administration World Meteorological Organization scales for calibration (NOAA-WMO-X2004A scale for CH_4, WMO-X2014A for CO and NOAA-2006A

145 for N_2O). These gas standards were recalibrated before, during and after the deployments to maintain traceability. The low-mixing ratio gas cylinder contained 298.5 ± 0.3 ppb of N_2O, 1692.4 ± 0.2 ppb of CH_4 and 119.1 ± 0.3 ppb for CO.

The high-mixing ratio gas cylinder contained 399.1 ± 0.3 ppb of N_2O, 2182.5 ± 0.3 ppb of CH_4 and 192.8 ± 0.5 ppb of CO, respectively. Detailed information on calibrations of the gas cylinders used during ATom are in Table S1 of the Supplement.

150   QCLS also measures carbon dioxide (CO_2) in a separate unit. Detailed information about QCLS CO_2 measurements can be found in Santoni et al. (2014).

2.2 Spectral analysis and calibration

The QCLS was damaged during shipping to the deployment site before the start of ATom-1 and the resulting alteration
155   in the optical alignment modified the sensitivity of the instrument to temperature and pressure changes during aircraft maneuvers. At a constant altitude, instrumental precision was similar to the precision measured during HIPPO (see Allan-Werle variance analysis in Fig. 2 in Santoni et al. 2014 for HIPPO and Fig. S3 for ATom), but drifts were observed during altitude changes due to the effects of changes in cabin temperature and pressure on the spectral location of interference fringes that arise in the optical path outside the sample cell. In addition, flight altitude changes could
160   mechanically stress the optical elements surrounding the cell, further modulating fringes or changing the shape of the detected laser intensity profile. These spectral artifacts ultimately reduced the accuracy of mixing ratios retrieved from spectral fitting. The spectral artifacts most strongly affected the measurements of CH_4 and N_2O. Several post-processing methods using the TDL-Wintel software were explored to improve the precision and accuracy of ATom QCLS N_2O data, most with little success. Since the measured spectra were all saved, it is possible to re-fit the data with different
165   fit parameters. A limited number of interference fringes may be included in the set of fitting functions. However, none of the previously used full re-fitting strategies significantly improved the data accuracy.

We have achieved significant improvement in the precision and accuracy of the QCLS N_2O data using a new method dubbed the "Neptune algorithm", developed by Aerodyne Research, Inc., and that has been further developed and applied to the data sets described here. The Neptune algorithm generates corrections to the mixing ratios retrieved
170   from the original fits by associating specific spectral features with anomalies in retrieved mixing ratios observed during calibrations, i.e. during intervals when the mixing ratios are held constant. The spectral baseline is defined as the spectral channels outside the boundaries of the spectral lines of the target gas. Fluctuations in the spectral baselines are quantified for the entire data set by means of principal component analysis (PCA). PCA provides an efficient description of the spectral fluctuations, naturally producing an ordered set from strongest to weakest of orthogonal vectors (spectral
175   forms), each with an amplitude history spanning the data set. The PCAs are defined by an optimization procedure during calibrations, when mixing ratio fluctuations are designed to be ~0. The finite fluctuations in retrieved mixing ratios during calibrations are fit in the spectral space of the baseline as linear combinations of the leading PCA vector amplitudes, creating a linear combination of amplitudes of spectral fluctuations that predict errors in the mixing ratios for each gas for an entire flight. The error-producing linear combination of amplitudes of PCA spectral fluctuations
180   produces a full set of anomaly estimates, which is subtracted from the retrieved mixing ratios during the flight. The

computational time for a 10-hour long dataset is only seconds, so variations in the algorithm's parameters (i.e. how many PCAs are retained) can be optimized rapidly.

The Neptune-PCA analysis improved the overall precision by a factor of 4 for CH_4 and a factor of 3 in the case of N_2O with respect to the precision of the original retrievals, as measured by the standard deviation of retrieved mixing ratios during calibrations. The repeatability of the retrieved calibrations was 0.2 ppb for N_2O and 1 ppb for CH_4 (Fig. S4). The laser path of the CH_4/N_2O laser was realigned between ATom-1 and -2 and the Neptune retrieval was applied to CH_4 and N_2O measurements corresponding to the ATom-2, -3 and -4 deployments. Mixing ratios of CH_4 and N_2O could not be retrieved during ATom-1 because light levels were too low for the CH_4/N_2O laser due to the damage-induced misalignment.

The steps involved in the Neptune correction process were as follows.

1) We paired the mixing ratio records with the corresponding spectra (1-s resolution) for each species (CH_4 and N_2O).

2) We grouped the mixing ratios and spectra by type as calibrations (zeros, low span and high span) and air samples, and in time. The spectral data were thus arranged in an array, with point number in the spectrum as x, and spectrum number as y. We calculated an average spectrum for each group type and subtracted these from each individual spectrum within a group.

3) We zeroed-out the spectral arrays at the positions of the absorption lines to concentrate on the fluctuations observed in the baseline and to prevent the PCA from finding line-depth fluctuations as relevant vectors during the calibrations. Some degree of smoothing (in x) was applied to the subtracted spectra, so that high-frequency fluctuations, which have little influence on the mixing ratio determination, are not represented. An example of such a processed spectral array is shown in Fig. 1a.

4) We applied PCA to the whole line-zeroed spectral array to evaluate the fluctuations. PCA is applied in two steps: multiply the spectral array by its transpose, to generate an autocovariance array; and then perform singular value decomposition on the autocovariance array. The PCA generated an efficient description of how the baseline of the spectrum changed with cabin pressure and temperature. The description of spectral fluctuations is made in terms of a set of products of vectors and amplitudes.

5) We fit the spectra to the PCAs to express mixing ratio fluctuations during the set of calibrations and zeros as a linear combination of PCA vector histories. The number of vector histories that we included in the fit typically is limited to less than 30, because the weaker PCA amplitudes tend to just describe random noise.

The linear combination of amplitudes that links spectral fluctuations in the baseline to mixing ratio fluctuations during calibrations, was then applied to the full data set. That generated the retrieval errors for uncalibrated mixing ratios, for the whole time series. We subtracted the errors from the initial retrievals from TDLWintel-QCLS software and computed calibrated mixing ratios using the corrected retrievals for both calibrations and samples. An example of the result of the Neptune algorithm on the N_2O samples and calibrations for the ATom-4 flight on 12 May 2018 is

215   shown in Fig. 1b. The approach used here to minimize the effect of changes in pressure and temperature in optical instruments is based on the observation of fluctuations of the baseline during calibrations. Hence, in those cases where altitude changes occurred during sampling but not during any of the calibrations for an individual flight, this methodology will not provide any improvement. Due to frequent calibrations, we did not observe this rare scenario in the whole mission. To evaluate the ultimate accuracy of our measurements we compare the QCLS N_2O measurements

220   with other on-board N_2O measurements as well as with the surface N_2O measurements of stations located along the flight tracks.

3 Accuracy of N_2O measurements from QCLS

We evaluated N_2O mixing ratios measured by QCLS against three other instruments measuring N_2O on the NASA DC-

225   8 aircraft during ATom. In addition, we compared the set of 4 airborne measurements to data from the flask sampling network at ground stations from the NOAA Global Monitoring Laboratory (GML, https://www.esrl.noaa.gov/gmd/) to evaluate the differences between the airborne data and the ground-based measurements in the NOAA reference network.

230   ### 3.1 Comparison between airborne N_2O measurements

Measurements of N_2O on the DC-8 were obtained by (i) the Unmanned Aircraft Systems Chromatograph for Atmospheric Trace Species (UCATS, Hintsa et al., 2021), (ii) the PAN and other Trace Hydrohalocarbon ExpeRiment (PANTHER; Moore et al., 2006; Wofsy et al., 2011), (iii) the Programmable Flask Package Whole Air Sampler (PFP; Montzka et al., 2019), and (iv) our 1-Hz QCLS.

235   We compared QCLS, PANTHER and UCATS in 10s intervals as provided in the merged file, MER10_DC8_ATom-1.nc, available at the Oak Ridge National Laboratory Distributed Active Archive Center (ORNL-DAAC, Wofsy et al., 2018, https://doi.org/10.3334/ORNLDAAC/1581). The file MER-PFP merged with the PFP sampling interval, also available in this repository, was used to compare QCLS and PFP data. The one-to-one comparison between these instruments showed an overall overestimation of N_2O mixing ratios from QCLS (see Fig.

240   2A1–2A3). The 95% confidence interval of the mean difference of the pairs (95% C.I.) was 0.75 ± 0.04 ppb between QCLS and PANTHER, 1.13 ± 0.03 ppb between QCLS and UCATS, and 1.18 ± 0.09 ppb between QCLS and PFP, respectively, for the full data set (ATom-2, -3 and -4). Information about the coefficients of the linear fit for each instrument comparison and the 95% C.I. of the difference for each pair are shown in Table of S2. The offset that QCLS N_2O shows against PFP N_2O coincides with the offset already reported by Santoni et al. (2014) during HIPPO in 2009-

245   2011, which may be attributed to our calibration procedure. PFP is the reference instrument on board, analyzed with excellent precision and accuracy.

3.2 Comparison between airborne and surface measurements of N₂O

We evaluate the traceability of lower-troposphere N_2O mixing ratios by ATom by comparing the four airborne
250   instruments with the surface measurements of N_2O from the NOAA flask sampling network at common sampling
locations. Information about the surface stations used here is shown in Table of S.3 of the Supplement.

A mean value of N_2O within a latitude range of 5 degrees north and south with respect the nearest surface station
and between 1 to 4 km altitude of instrument was compared with the mean N_2O at the station located within that latitude
grid and +/- 5 days of the flight (due to the non-daily frequency of flask samples). We chose this altitude range to agree
255   with the low free troposphere conditions that characterized most of the selected ground stations. The comparison of the
whole data set (ATom-2, -3, -4) shows an overall overestimation of N_2O mixing ratios by QCLS and PANTHER with
respect surface data of 1.37 ± 0.35 and 0.44 ± 0.51 ppb (95% C. I.), respectively. In contrast, UCATS and PFP showed
0.27 ± 0.37 and 0.008 ± 0.34 ppb (95% C. I.), underestimation with respect to the surface data, respectively (Fig.2B1-
2B4). Due to the great agreement between PFP and the surface stations and the consistent offset that QCLS shows
260   against PFP and the stations, in the following sections, QCLS N_2O dataset is corrected by subtracting the offset with
respect to the PFP data on-board in each deployment: 1.03 ± 0.13 ppb in AT-2, 1.49 ± 0.19 ppb in AT-3, and $1.18 \pm$
0.17 ppb in AT-4.

These results show the very close comparability of ATom airborne N_2O instruments (differences < 0.5 ppb, 0 ppb in
265   the case of PFP) relative to the surface stations and demonstrate the feasibility of using ATom N_2O measurements to
evaluate the impact of stratospheric air and meridional transport of N_2O emissions in N_2O tropospheric column
measurements over the ocean basins. In the following section, we define the boundary conditions based on the NOAA
Greenhouse Gas Marine Boundary Layer Reference from the NOAA GML Carbon Cycle Group (NOAA/ESRL GML
CCGG, https://www.esrl.noaa.gov/gmd/ccgg/mbl/) for evaluating the impact of stratospheric air and meridional
270   transport of N_2O emissions in N_2O tropospheric column over the ocean basins. The NOAA-MBL N_2O product is
synthetic   latitude   profile   generated   at   0.05   sine   latitude   and   weekly   resolution
(https://www.esrl.noaa.gov/gmd/ccgg/mbl) from individual flask measurements of marine boundary-layer surface
stations distributed along the two ocean basins, and provides the scenario to evaluate the traceability of aircraft
measurements relative to ground measurements in remote sites (https://doi.org/10.15138/53g1-x417).

275

4. Results and Discussion

The vertical profiles of N_2O from ATom provide a global overview of the N_2O distribution in the troposphere with
observations over the Pacific and Atlantic basins. For this study we do not include data collected over and close to land.
In ATom, N_2O ranged between 280 and 335 ppb over the oceans. In each season, the lowest N_2O mixing ratios are
280   observed at high latitudes (HL, > 60°) in the UT/LS (8–12.5 km) in air transported downward from the stratosphere.

The highest N_2O mixing ratios are found close to the equator (30° S–30° N, 326 to 335 ppb), extending along the tropospheric column up to 6 km and influenced by convective activity over the tropical regions (Kort et al., 2011; Santoni et al., 2014). At mid-latitudes (ML, 30°–60° N), tropospheric N_2O values ranged between 322 and 333 ppb. Tropospheric N_2O tends to increase towards northern latitudes as a result of higher anthropogenic emissions in the

285 Northern Hemisphere relative to the Southern Hemisphere. More details on the variability of N_2O mixing ratios along the tropospheric column are described in Section S1.

We study the impact of N_2O sources and stratospheric air on the N_2O column based on the anomalies (enhancements and depletions) we observed in the airborne N_2O mixing ratios relative to the N_2O "background" defined here as the NOAA-MBL product. We use the NOAA-MBL product to constrain a latitudinal gradient of N_2O mixing

290 ratios at the surface for each deployment. These data and have been widely used to estimate the N_2O background (Assonov et al., 2013; Nevison et al; 2011). More information about the NOAA-MBL product and the latitudinal gradient of their measurements is discussed in Section S2. This approach highlights the extra information that aircraft profiles can provide. Cross-sections of N_2O anomalies are shown in Fig. 3. The data describe the overall homogeneity of N_2O in the troposphere (30% of the anomalies ranged between ± 0.5 ppb). We consider the ± 0.5 ppb interval to

295 account for the day-to-day and seasonal variability of N_2O. Episodes of N_2O depletion (< -0.5 ppb) related to the influence of stratospheric air are observed in 53.5% of the aircraft samples during ATom-2 to -4, whereas episodes of N_2O enhancement (> 0.5 ppb) related to the contribution of N_2O sources account for 16.5% of the observed anomalies.

4.1 Impact of stratospheric air on tropospheric N_2O mixing ratios during ATom

300 We observed a strong depletion in N_2O mixing ratios during October 2017 at high southern latitudes (SH, Fig. 3c), when the Antarctic polar vortex has broken up and the period of maximum stratosphere-to-troposphere transport was ending at Northern high latitudes. Polar vortex break-up allows depleted levels of N_2O to be distributed and to persist in the troposphere. During February 2017, 35% of the N_2O observations over the Atlantic were lower than seasonal background defined from the NOAA-MBL product (i.e., N_2O differences < -0.5 ppb) and 51% over the Pacific. During

305 October 2017, depleted N_2O accounted for 55% of the observations over the Atlantic and 46% over the Pacific, whereas during May 2018, the percentage was 53% and 49% in the Atlantic and Pacific basins, respectively. In the Arctic, the strongest signal of N_2O depletion above the surface was observed in May. These results support previous work suggesting that downward transport of stratospheric air with low N_2O exert a strong influence on the variance of tropospheric N_2O mixing ratios (Nevison et al., 2011; Assonov et al, 2013). Bands of depleted N_2O begin to reach the

310 surface in March-April in the Southern Hemisphere (ATom-4, Fig. 3b and e) arriving as late as August-September in the Northern Hemisphere (ATom-3 Fig. 3c and f). Surface seasonal minima therefore occur 2–4 months later than the polar vortex break-up (see Fig. S9 and S10) (*cf.* Nevison et al., 2011 and references therein).

The impact of stratosphere-to-troposphere transport can be studied by combining information on N_2O with other chemical tracers such as carbon monoxide (CO from QCLS), sulfur hexafluoride (SF_6 from PANTHER), ozone (O_3

315   from the NOAA - NOyO3; Bourgeois et al., 2020) and CFC-12 (from PANTHER), as well as meteorological parameters such as potential vorticity, the product of absolute vorticity and thermodynamic stability (PV, generated by GEOS5-FP for ATom). The correlation of N_2O with CO shows an L-shape curve similar to those typically observed on O_3-CO correlations during events of stratosphere-to-troposphere airmass mixing (Fig. 4b, Krause et al., 2018). The slightly higher mixing ratios of CO, N_2O and SF_6 in the Northern Hemisphere are due to the larger emissions in this hemisphere.

320   Tropospheric N_2O can be identified as the horizontal band containing high N_2O (> 328 ppb) and variable CO and SF_6, whereas the vertical band with variable N_2O and small changes in CO and SF_6, shows the stratospheric influence (Fig. 4a–d). The range of N_2O-CO mixing lines are indicative of the time scales of the mixing events, where straight mixing lines are due to fast mixing time scales (Krause et al., 2018). Episodes of fast air mass mixing were observed during all deployments (see tracer-to-tracer correlations from the three deployments in Fig. S11). At the Pacific northern mid and

325   high latitudes (NMHL > 30º N), we found a consistent linear relationship between N_2O and O_3, with a relatively constant N_2O/O_3 slope (-0.05 to -0.04) during all seasons. Linear correlations between N_2O and CFC-12 highlight the dominant influence of stratospheric air depleted in these two substances in the range of mixing ratios observed at mid and high latitudes.

During spring, the mid-latitudes are strongly impacted by stratospheric air due to the occurrence of tropopause

330   folds (also known as cut-off lows) to the south of the westerlies (Hu et al., 2010 and references therein). The stronger depletion of N_2O mixing ratios observed over the Atlantic relative to the Pacific during spring is due to a greater number of deep stratosphere-to-troposphere transport events at middle latitudes in the region between May and July (Fig. 3e; Cuevas et al., 2013 and references therein). Anomalies in PV relative to its mean latitudinal distribution in the free troposphere (2–8 km) highlight events of strong downward transport of stratospheric air. Negative PV, N_2O, CO, and

335   CFC-12 anomalies (positive for O_3) describe the transport of stratospheric air into the troposphere in the SH, whereas positive PV and negative N_2O, CO, and SF_6 anomalies (positive for O_3) describe the downward transport of stratospheric air in the NH (Fig. 4e-h). The correlations between N_2O and PV, and the similarities with CFC-12, indicate that stratosphere-to-troposphere exchange leads to variations of tropospheric N_2O up to 10 ppb in the higher latitudes for the altitudes covered during the flights. This influence is notably larger than the 2–4 ppb enhancements associated

340   with regional emissions (see below).

4.2 Impact of emissions on tropospheric N_2O mixing ratios during ATom

During ATom, episodes of N_2O positive anomalies relative to the surface station MBL reference occur close to the equator (Fig. 3a-c), and in a few locations at mid latitudes, in both ocean basins across all seasons. We use the

345   information from the vertical profiles including back-trajectories and correlated chemical tracers to trace the origins of these enhancements including: CO, CH_4, and CO_2, measured by the QCLS and NOAA Picarro 2401-m, hydrogen cyanide (HCN), sulfur dioxide (SO_2), hydrogen peroxide (H_2O_2) and peroxyacetic acid (PAA) measured with the Chemical Ionization Mass Spectrometer (CIT-CIMS, St. Clair et al., 2010), ammonium (NH_4^+), sulfate (SO_4^{2-}) and

nitrate (NO_3^-) and organic aerosols (OA) from the CU Aircraft High-Resolution Time-of-Flight Aerosol Mass
350   Spectrometer (HR-AMS, DeCarlo et al., 2006; Canagaratna et al., 2007; Jimenez, et al., 2019; Guo et al., 2020; Hodzic, et al., 2020), NOy from the NOAA NOyO3 4-channel chemiluminescence (CL, Ryerson et al., 2019), CH_2Br_2, CH_3CN, benzene and propane from the Trace Organic Gas Analyzer (TOGA, Apel et al., 2019) instrument, and atmospheric potential oxygen (APO ≈ O_2 + 1.1 x CO_2) from the NCAR Airborne Oxygen Instrument (AO2, Stephens et al., 2020).

Trajectories and associated surface influence functions were computed using the Traj3D model (Bowman, 1993)
355   and wind fields from the National Center for Environmental Prediction Global Forecast System (NCEP GFS). Model trajectories were initialized at receptors spaced one minute apart along the ATom flight tracks, and followed backwards for 30 days, and reported at 3-hour resolution. From these trajectories we calculated the surface influence for each receptor point (footprints in units of ppt/(nmol m^{-2} s^{-1})).

We calculate the correlations between N_2O and the mentioned species considering three arbitrary layers (0-2000
360   m, 2000-4000 m, and 4000-6000 m). Correlation coefficients in each layer for a given profile were calculated using a minimum threshold of 15 data points per layer. These profiles show that many of the most prominent enhancements of N_2O are closely associated with pollutants such as HCN, CH_3CN, H_2O_2, and other pollutants associated with combustion and photochemical air pollution. Some profiles show peaks closely correlated with SO_2 and enhanced PM1 particles, and vertical gradients were sometimes correlated with gradients of APO and HCN.

365   The best predictors for N_2O peaks in many cases were H_2O_2 and PAA. These are both primary pollutants and the end products of atmospheric photochemistry. For the altitude range 2–4 km, regressions produced $r^2 > 0.7$ for 16 profiles of N_2O vs. H_2O_2 and 15 profiles of N_2O vs. HCN (a tracer for combustion), but only three such profiles produced these strong associations for both H_2O_2 and HCN in common. Hence, H_2O_2 appears to be an independent predictor for N_2O enhancements in polluted air encountered over the remote oceans. This result raises the question as to whether globally
370   significant production of N_2O may be occurring in heterogeneous reactions involving HONO, NO_2, or NO redox chemistry nearby to strong sources of reactive pollutants, as has been observed in heavily polluted atmospheres (Wang et al., 2020), or as theorized to occur in the plumes of refineries or power plants (e.g. Pires and Rossi, 1997).

In most of the cases, because we were sampling in the middle of the oceans and not over the source regions, the distinction between the different sources contributing to the observed N_2O enhancements is not possible. In this analysis
375   we also observe that the impact of the different sources to N_2O mixing ratios is regionally dependent. Thus, in the following lines we describe with some examples, the sources contributing to the major enhancements of N_2O observed during ATom by oceanic regions, though we cannot pinpoint precisely the source processes.

4.2.1 N_2O enhancements over the Pacific

380   Episodes of N_2O enhancements were frequently observed at the southern Pacific Ocean mid latitudes, linked by the associated footprints to emissions over the continents. In this region, N_2O enhancements are predominantly correlated with enhancements on H_2O_2, PAA and CO. For example, consider Fig. 5 showing data from profile 12 on 3 May 2018,

at 49.5–50° S near the Dateline. A distinct peak in N_2O of 1 ppb amplitude, at 1700 m altitude, is significantly correlated with enhancements in CH_3CN. These associations and the footprints suggest a regional contribution from fuel types

385   from the industrial zone of Australia (Fig. 5c). At higher altitudes (2.5–6 km), strong correlations between N_2O, H_2O_2, PAA, CO and HCN, but not SO_2, suggest the influence of biomass burning from central Australia (3–5 km) and from South America (6 km) (Fig. 5b and 5c middle and right panels, and Fig. S11f). The relatively low mixing ratios of short-lived trace gases, and the surface influence based on the back trajectories (Fig. S13a), indicate that most of these profiles sampled significantly aged air masses transported for extended periods over the South Pacific.

390   At the equatorial Pacific, episodes of N_2O enhancements were frequently associated with a mixture of potential marine, industrial and biomass burning emissions. Atmospheric potential oxygen (APO) is a tracer primarily of oxygen exchange with the oceans, defined as deviations in the oxygen-to-nitrogen ratio ($\delta(O_2/N_2)$) corrected for changes in O_2 due to terrestrial photosynthesis and respiration, and also mostly for influences from combustion (Stephens et al., 1998),

395                 $\delta APO = \delta(O_2/N_2) + 1.1 / X_{O2} (X_{CO2} - 350)$ (1)

Here $\delta(O_2/N_2)$ is the deviation in O_2:N_2 ratio (per meg), 1.1 is an approximation to the O_2:CO_2 ratio for photosynthesis and respiration, X_{O2} is the mole fraction of O_2 in dry air, and X_{CO2} is the mole fraction of CO_2 in the air sample (dry, $\mu mol\ mol^{-1}$). Since APO primarily tracks oxygen exchange between the ocean and the atmosphere,

400   depletions in APO can indicate marine N_2O emissions from areas with strong upwelling (Leuker et al., 2003; Ganesan et al., 2020). However, APO is also sensitive to pollution such as biomass burning and fossil fuel combustion (Lueker et al., 2001) and because both N_2O and APO have meridional gradients resulting from many influences, correlations can result simply from sampling air transported from different latitudes. In ATom, 9 profiles showed significant correlations ($r^2 > 0.7$) between N_2O and APO (or $\delta(O_2$:$N_2)$, which has lower measurement noise), for altitude bins 0–2

405   km (8) and 2–4 km (1) where backtrajectories trace their origin close to the North American west coast and the Mauritanian coast, and in the equatorial Pacific. The median slope of regressions of APO vs. N_2O for these profiles in ATom was -0.04, and the mean -0.05 (± 0.04, 1σ) ppb per meg, very similar to the range found by Ganesan et al. (2020) and Leuker et al. (2003) in coastal areas.

   An example is shown in Fig. 6 for 1 May 2018. We observed high correlation between N_2O and APO ($r^2 = 0.66$)

410   between 0 and 4 km altitude. At these altitudes we also see enhancements in dibromomethane (CH_2Br_2), a tracer of phytoplankton biomass (Liu et al., 2013 and references therein), consistent with a marine biological flux of halogenated VOCs (Asher et al., 2019), dimethyl sulfide (DMS) and methanesulfonic acid (MSA), main particulate product of DMS oxidation in the MBL. On this flight, the footprints and the surface ocean influence (Fig. S12b) indicate that this gradient represents a difference in sampling a marine airmass from the south near the surface and a more continentally influences

415   air mass from the east at 4 km (Fig. 6A–C). Thus, the N_2O:APO correlation most likely represents the latitudinal and ocean-land gradients established for a combination of reasons, with higher APO and lower N_2O from higher southern

latitudes away from continents. In this particular flight, N_2O variations were more noticeable between 4 and 6 km height, in relation to biomass burning plumes from fires occurring in Venezuela and the Caribbean, in agreement with simultaneous enhancements on CO, HCN mixing ratios (Fig. 6A, C and Fig. S12), and pollution sources near coastlines.

420

4.2.2 N_2O enhancements over the Atlantic

The Atlantic basin ATom flights saw much more continental influence than the Pacific. Around 30° N, in the North Atlantic during winter, we observe small enhancements of N_2O that contrasts with the overall influence of stratospheric air on the tropospheric column (AT-2, Fig. 3d). The contribution is much higher during the fall season

425 (AT-3, Fig. 3f). Several episodes of N_2O enhancements are associated with enhancements of CH_4, CO, and HCN. At this altitude range, we also observe some episodes where N_2O increases while CO_2 decreases (figure not shown), which could reflect the accumulation of agricultural emissions over the summer or just greater sampling of Northern Hemisphere summer air masses, whereas increases of N_2O with CO are indicators of urban pollution and together with HCN are associated with a few episodes of biomass burning.

430 The influence of different regions on the N_2O mixing ratios over the Atlantic is shown on 14 May 2018 (Fig. 7). This profile shows the contribution to tropospheric N_2O from western Europe pollution transported down over the Mauritanian coast, combined with biomass burning emissions, urban and industrial emissions from southern Africa and the Middle East (between 2 and 4 km), and polluted air masses from South America and the African west coast mixed with the oceanic contribution to N_2O (~10 km, Fig. 7A–C and Fig. S13). At high altitudes, N_2O enhancements are

435 caused by the interception of polluted airmasses from South America and the African west coast mixed with the oceanic contribution to N_2O (~10 km). The N_2O:APO correlations for the feature at 2 km most likely represent depletion of APO by industrial combustion, stoichiometrically consistent with the observed increases in CO_2 and CH_4 for this feature.

During ATom, we observed large contributions to tropospheric N_2O over the Atlantic Ocean from Africa, with

440 some influence from Europe and South America. In the subtropical and tropical regions over the Atlantic during AT-2, we found strong correlations between N_2O and H_2O_2 and PAA, HCN, CO, CO_2, SO_2, OA, NH_4^+ and SO_4^{2-} between 2 and 4 km, representing the combined influence of photochemistry ($r_{N2OvsPAA}^2 = 0.94$), biomass burning events from the Congo region ($r_{N2OvsHCN}^2 = 0.95$) and industrial production of N_2O from oil and gas emissions from the Niger River Delta in Africa ($r_{N2OvsSO2}^2 = 0.84$). An example is shown in Fig 8 for 15 February 2017 (Fig. S12 and land contribution

445 in Fig. S13).

To evaluate the origin of these enhancements, we combined the calculated surface influence with the monthly mean estimates of the global anthropogenic emission inventory from the Emissions Database for Global Atmospheric Research (EDGAR, http://edgar.jrc.ec.europa.eu/). By using a profile specific background, we can calculate the N_2O enhancement for a given profile. When the N_2O enhancement from the African outflow shown in Figure 8 is compared

450 with the emission inventory (Figure 9, bars represent the range of N_2O expected from variations in the background

choice), we see the largest influence from African agriculture (peaking at 2 ppb at 2 km), with smaller but significant influence from Asia and Europe (0.5 ppb each at 2-4 km). Not forgetting that we are comparing a single aircraft pass with a monthly mean estimate from the inventory, and the strong impact of the latitudinal gradient we observed on the N_2O data for this particular profile, the overall expected atmospheric enhancement of N_2O calculated from EDGAR for

455 the African region is in the order of magnitude than that observed in the atmosphere (if the error in our measurements is taken into account). EDGAR major contributions to these enhancements are agriculture soil emissions and industrial chemical processes (Fig. S14). High correlations between N_2O and HCN ($r^2 = 0.95$), CO and CH_3CN suggest a source of N_2O from burning emissions also contribute to the N_2O enhancement (Fig. 8 and Fig. S12). However, when these contributions are compared with the monthly mean fire contributions from the Global Fire Emissions Database (GFED,

460 https://www.globalfiredat.org), the GFED wildfire contributions are minimal (~0.2 ppb), suggesting fires of anthropogenic origin might be the source of that contribution (Fig. 8A–C, 9, and S11, and S13).

5. Conclusions

465 Highly resolved N_2O mixing ratios were obtained during the NASA ATom airborne program by applying a new spectral retrieval method to account for the pressure and temperature sensitivity of quantum cascade laser spectrometers when deployed on aircraft. This method improved the precision of our N_2O measurements by a factor of 3, allowing us to recover the precision of N_2O measurements to the level shown in previous aircraft missions.

The N_2O altitude profiles observed during ATom show that tropospheric N_2O variability is strongly driven by the

470 influence of stratospheric air depleted in N_2O, especially at middle and high latitudes. At high latitudes, our profiles showed a strong depleted N_2O signal around the time of the vortex break-up season, persisting for several months. Combining the information from N_2O profiles and other chemical tracers such as CO, SF_6, O_3 and CFC-12 we traced the propagation of stratospheric air along the tropospheric column down to the surface. This transport dominates the N_2O seasonal cycle and creates the seasonal surface minima 2–3 months after the peak stratosphere-troposphere

475 exchange in spring.

The high resolution of this data set (10 s) allowed us to study the factors influencing the enhancements in the N_2O tropospheric mixing ratios associated with biomass burning, human activities such as urban and industrial emissions. The highest N_2O mixing ratios are close to the Equator, extending through the tropospheric column. Episodes of the strongest N_2O enhancements were observed close to the Equator and also in a number of locations at mid-latitudes. We

480 use the information given by the vertical profiles of N_2O and a variety of chemical tracers together with footprints computed every 60 s along the flight track to identify and trace the sources of these N_2O enhancements. N_2O enhancement events were more frequent in the Atlantic than in the Pacific.

Over the Atlantic, excess N_2O together with the co-occurrence of other pollutants suggested that industrial and urban N_2O emissions originated in distant locations such as western and southern Africa, the Middle East, Europe and

485   South America may be significantly greater than the emissions from biomass burning in Africa. This view is supported by our observations of a strong contribution to N$_2$O from oil and gas emissions from the Niger River Delta in Africa. Possibly the correlations observed between N$_2$O and SO$_2$ (r^2 = 0.90) could be used to estimate N$_2$O emissions from oil and gas.

Over the southern Pacific Ocean and the tropical Atlantic Ocean, we observed a significant number (>12) of
490   profiles where peaks in N$_2$O correlated very closely with H$_2$O$_2$ and PAA, and notably less well with HCN or CO. Since H$_2$O$_2$ and PAA are endpoint products of photochemical pollution, this observation raised the question as to whether significant N$_2$O may be produced by heterogenous processes involving HONO or NO$_x$ reactions in acidic aerosols close to sources, or in very heavily polluted areas. It is hard to make a definite conclusion based on measurements so far from the most active regions. Studies directed at understanding this question would have to be carried out directly in the
495   polluted areas. Because agricultural activities do not have unique tracer signatures, we were not able to distinguish contributions from cultivated and natural soils to N$_2$O emissions from the ATom data. Previous airborne studies have observed these inputs, using flights in the main agricultural areas (Kort et al, 2008), and at towers in these regions (e.g., Nevison et al, 2017; Miller et al., 2008).

Our study shows that airborne campaigns such as ATom can help trace the origins of biomass burning and industrial
500   emissions and investigate their impact on the variability of tropospheric N$_2$O, providing unique signatures in vertical profiles and with covariate tracers. We hope that the information provided by the global, highly resolved N$_2$O profiles from the ATom mission will help better diagnose and reduce uncertainties of atmospheric chemical transport models for constraining the N$_2$O global budget.

505

Appendix A: List of frequently used symbols and acronyms

Description	*Acronym*
Atmospheric Potential Oxygen	APO
Atmospheric Tomography	ATom
California Institute of Technology - Chemical Ionization Mass Spectrometer	CIT-CIMS
CU Aircraft High-Resolution Time-of-Flight Aerosol Mass Spectrometer	HR-AMS
Global Monitoring Laboratory	GML
HIAPER Pole-to-Pole Observations	HIPPO
High Latitudes	HL
HIgh-resolution TRANsmission molecular absorption database	HITRAN
Marine Boundary Layer	MBL
Middle Latitudes	ML
Modern-Era Retrospective analysis for Research and Applications 2 model	MERRA2
National Center for Environmental Prediction Global Forecast System model	NCEP GFS
National Oceanic and Atmospheric Administration	NOAA
NCAR Airborne Oxygen Instrument	AO2
NOAA Halocarbons and other Atmospheric Trace Species Flask Sampling Program	NOAA-HATS

NOAA NOyO₃ 4-channel chemiluminescence	CL
525 Northern Hemisphere	NH
PAN and other Trace Hydrohalo-carbon ExpeRiment	PANTHER
Particle Analysis by Laser Mass Spectrometry instrument	PALMS
Potential Vorticity	PV
Principal Component Analysis	PCA
530 Programmable Flask Package Whole Air Sampler	PFP
Quantum Cascade Laser Spectrometer	QCLS
Southern Hemisphere	SH
Stochastic Time-Inverted Lagrangian Transport Model	STILT
Trace Organic Gas Analyzer	TOGA
535 Unmanned Aircraft Systems Chromatograph for Atmospheric Trace Species	UCATS
Upper Troposphere/Lower Stratosphere	UT/LS
World Meteorological Organization	WMO

540   *Data availability.* Data from the ATom mission can be found on the NASA ESPO archive (https://espoarchive.nasa.gov) at https://espoarchive.nasa.gov/archive/browse/atom, and in the ATom data repository at the NASA/ORNL DAAC: https://doi.org/10.3334/ORNLDAAC/1581 (Wofsy et al., 2018).

545   *Supplement.* The supplement related to this article is available on-line at: https://doi.org/xx.xxxx/acp-20-xxx-2020-supplement.

Author Contribution. Y. Gonzalez did the data analysis and wrote and revised the paper. S.C. Wofsy and R. Commane
550   actively contributed to the design of the study and data analysis. J.B. MacManus designed the Neptune software for spectral re-analysis and contributed to the writing. R. Commane and B.C. Daube performed and analyzed QCLS measurements of CH₄, N₂O and CO and contributed to the discussions. E. Manninen and L. Schiferl contributed to the data analysis. K. McKain performed and analyzed NOAA Picarro measurements of CH4, CO and CO₂. J.W. Elkins, E.J. Hintsa and F. Moore performed and analyzed N₂O, SF₆ and CFC-12 measurements from PANTHER and UCATS
555   instruments. F. Moore, , S. Montzka and C. Sweeney performed and analyzed N₂O measurements with the Programmable Flask Package Whole Air Sampler (PFP). P. O. Wennberg, J. Crounse, M. Kim and H. M. Allen performed and analyzed CIT-CIMS measurements of HCN and SO₂ shown here. K. Froyd performed and analyzed PALMS measurements. J.L. Jimenez, P. Campuzano-Jost and B. A. Nault performed and analyzed HR-AMS spectrometer of a variety of aerosols. E. Ray provided backtrajectories for each minute during the flight tracks and P.
560   Newman provided the GEOS5 FP meteorological products. T.B. Ryerson, I. Bourgeois, J. Peischl and C. R. Thompson performed and analyzed NOyO₃ measurements of NOy and O₃. B .B. Stephens and E. J. Morgan performed and

analyzed AO2 and the Medusa Whole Air Sampler measurements of O_2/N_2 and CO_2 and assisted with the interpretation. E. C. Apel and R. S. Hornbrook performed and analyzed TOGA measurements of volatile organic compounds. All coauthors provided comments on the paper.

565

Competing interests. The authors declare no conflict of interest

570 *Acknowledgements.* We would like to thank the ATom leadership team, science team, the NASA DC-8 pilot, technicians, and mechanics for their contribution and support during the mission. We thank Karl Froyd for the aerosol products during ATom that support this study. This work has been funded by ATom (grant agreement number NNX15AJ23G) and the Base Funding AURA (grant agreement number NNX17AF54G). This material includes work supported by the National Center for Atmospheric Research, which is a major facility sponsored by the National Science

575 Foundation under Cooperative Agreement No. 1852977). LS and RC were supported by NASA grant NNX15AG58A and Columbia University. JLJ, BAN and PCJ were supported by NASA grants NNX15AH33A and 80NSSC19K0124. The AO2 measurements were supported by NSF AGS-1547626 and AGS-1623745.

580 **References**

Albanito, F., Lebender, U., Cornulier, T., Sapkota, T. B., Brentrup, F., Stirling, C., and Hillier, J.: Direct Nitrous Oxide Emissions from Tropical and Sub-Tropical Agricultural Systems - A Review and Modelling Of Emission Factors, Sci. Rep., 7, 44235, doi: 10.1038/srep44235, 2017.

585 Apel, E., Asher, E. C., Hills, A. J. and Hornbrook, R. S.: ATom: L2 Volatile Organic Compounds (VOCs) from the Trace Organic Gas Analyzer (TOGA), ORNL DAAC, https://doi.org/10.3334/ORNLDAAC/1749, 2019.

Asher, E., Hornbrook, R. S., Stephens, B. B., Kinnison, D., Morgan, E. J., Keeling, R. F., Atlas, E. L., Schauffler, S. M., Tilmes, S., Kort, E. A., Hoecker-Martínez, M. S., Long, M. C., Lamarque, J.-F., Saiz-Lopez, A., McKain, K., Sweeney, C., Hills, A. J., and Apel, E. C.: Novel approaches to improve estimates of short-lived halocarbon

590 emissions during summer from the Southern Ocean using airborne observations, Atmos. Chem. Phys., 19, 14071–14090, https://doi.org/10.5194/acp-19-14071-2019, 2019.

Bourgeois I., Peischl, J., Thompson, C. R., Aikin, K. C., Campos, T., Clark, H., Commane, R., Daube, B., Diskin, G. W., Elkins, J. W., Gao, R.-S., Gaudel1, A., Hintsa, E. J., Johnson, B. J., Kivi, R., McKain, K., Moore, F. L., Parrish, D. D., Querel, R., Ray, E., Sánchez, R., Sweeney, C., Tarasick, D. W., Thompson, A. M., Thouret, V., Witte, J. C.,

595 Wofsy, S. C. and Ryerson, T. B.: Global-scale distribution of ozone in the remote troposphere from ATom and HIPPO airborne field missions, Atmos. Chem. Phys., 20, 10611–10635, https://doi.org/10.5194/acp-20-10611-2020, 2020.

Bowman, K. P.: Large-scale isentropic mixing properties of the Antarctic polar vortex from analyzed winds, J. Geophys. Res. Atmos., 98(D12), 23, 013, https://doi.org/10.1029/93JD02599, 1993.

600 Brock, C. A., Williamson, C., Kupc, A., Froyd, K. D., Erdesz, F., Wagner, N., Richardson, M., Schwarz, J. P., Gao, R.-S., Katich, J. M., Campuzano-Jost, P., Nault, B. A., Schroder, J. C., Jimenez, J. L., Weinzierl, B., Dollner, M., Bui, T., and Murphy, D. M.: Aerosol size distributions during the Atmospheric Tomography Mission (ATom): methods,

uncertainties, and data products, Atmos. Meas. Tech., 12, 3081–3099, https://doi.org/10.5194/amt-12-3081-2019, 2019.

605   Butterbach-Bahl, K., Baggs, E. M., Dannenmann, M., Kiese, R., and Zechmeister-Boltenstern, S.: Nitrous oxide emissions from soils: how well do we understand the processes and their controls? Phil. Trans. R. Soc. B, 368, 20130122, https:// doi.org/10.1098/rstb.2013.0122, 2013.

Canagaratna, M. R., Jayne, J. T., Jimenez, J. L., Allan, J. D., Alfarra, M. R., Zhang, Q., Onasch, T. B., Drewnick, F., Coe, H., Middlebrook, A., Delia, A., Williams, L. R., Trimborn, A. M., Northway, M. J., Decarlo, P. F., Kolb, C.
610   E., Davidovits, P. and Worsnop, D. R.: Chemical and microphysical characterization of ambient aerosols with the Aerodyne Aerosol Mass Spectrometer, Mass Spectrom. Rev., 26(2), 185–222, 2007.

Castaldi, S., de Grandcourt, A., Rasile, A., Skiba, U., and Valentini, R.: CO_2, CH_4 and N_2O fluxes from soil of a burned grassland in Central Africa, Biogeosciences, 7, 3459–3471, https://doi.org/10.5194/bg-7-3459-2010, 2010.

Castaldi, S., Ermice, A., Strumia, S.: Fluxes of N_2O and CH_4 from soils of savannas and seasonally-dry ecosystems, J.
615   Biogeogr., 33, 401–415, https://doi.org/10.1111/j.1365-2699.2005.01447.x, 2006.

Crounse, J. D., McKinney, K. A., Kwan, A. J. and Wennberg, P. O.: Measurement of Gas-Phase Hydroperoxides by Chemical Ionization Mass Spectrometry, Anal. Chem., 78, 19, 6726–6732, https://doi.org/10.1021/ac0604235, 2006.

Cuevas, E., González, Y., Rodríguez, S., Guerra, J. C., Gomez-Peláez, A. J., Alonso-Pérez, S., Bustos, J., and Milford,
620   C.: Assessment of atmospheric processes driving ozone variations in the subtropical North Atlantic free troposphere, Atmos. Chem. Phys., 13, 1973–1998 , https://doi.org/10.5194/acp-13-1973-2013, 2013.

DeCarlo, P. F., Kimmel, J. R., Trimborn, A., Northway, M. J., Jayne, J. T., Aiken, A. C., Gonin, M., Fuhrer, K., Horvath, T., Docherty, K. S., Worsnop, D. R. and Jimenez, J. L.: Field-deployable, high-resolution, time-of-flight aerosol mass spectrometer, Anal. Chem., 78(24), 8281–8289, 2006.

625   Forster, P., Ramaswamy, V., Artaxo, P., Berntsen, T., Betts, R., Fa- hey, D. W., Haywood, J., Lean, J., Lowe, D. C., Myhre, G., Nganga, J., Prinn, R., Raga, G., Schulz, M., and Van Dorland, R.: Changes in Atmospheric Constituents and in Radiative Forcing, in: Climate Change 2007: The Physical Science Basis. Contribution of Working Group I to the Fourth Assessment Report of the Intergovernmental Panel on Climate Change, Cambridge University Press Cambridge, UK and New York, NY, USA, 2007.

630   Froyd, K., Murphy, D., Sanford, T. J., Thomson, D. S., Wilson, J., Pfister, L. and Lait, L. R.: Aerosol composition of the tropical upper troposphere, Atmos. Chem. Phys., 9, 4363-4385, https://doi.org/10.5194/acp-9-4363-2009, 2009.

Ganesan, A. L., Manizza, M., Morgan, E. J., Harth, C. M., Kozlova, E., Lueker, T., Manning, A. J., Lunt, M.F., Mühle, J., Lavric, J. V., Heimann, M., Weiss, R. F. and Rigby, M.: Marine Nitrous Oxide Emissions From Three Eastern
635   Boundary Upwelling Systems Inferred From Atmospheric Observations, Geophysical Research Letters, 47, e2020GL087822, https://doi.org/10.1029/2020GL087822, 2020.

Guo, H., Campuzano-Jost, P., Nault, B. A., Day, D. A., Schroder, J. C., Dibb, J. E., Dollner, M., Weinzierl, B. and Jimenez, J. L.: The Importance of Size Ranges in Aerosol Instrument Intercomparisons: A Case Study for the ATom Mission, Atmos. Meas. Tech. Disc., doi:10.5194/amt-2020-224, 2020.

640   Hintsa, E., Boering, K. A., Weinstock, E. M., Anderson, J. G., Gary, B. L., Pfister, L., Daube, B. C., Wofsy, S. C., Loewenstein, M., Podolske, J. R., Margitan, J. J., and Bu, T. T.: Troposphere-to-stratosphere transport in the lowermost stratosphere from measurements of H_2O, CO, N_2O and O_3, Geophys. Res. Lett., 25, 14, 2655-2658, https://doi.org/10.1029/98GL01797, 1998.

Hintsa, E. J., Moore, F. L., Hurst, D. F., Dutton, G. S., Hall, B. D., Nance, J. D., Miller, B. R., Montzka, S. A., Wolton,
645   L. P., McClure-Begley, A., Elkins, J. W., Hall, E. G., Jordan, A. F., Rollins, A. W., Thornberry, T. D., Watts, L. A., Thompson, C. R., Peischl, J., Bourgeois, I., Ryerson, T. B., Daube, B. C., Pittman, J. V., Wofsy, S. C., Kort, E., Diskin, G. S., and Bui, T. P.: UAS Chromatograph for Atmospheric Trace Species (UCATS) – a versatile instrument for trace gas measurements on airborne platforms, Atmos. Meas. Tech. Discuss., https://doi.org/10.5194/amt-2020-496, in review, 2021.

650   Hodzic, A., Campuzano-Jost, P., Bian, H., Chin, M., Colarco, P. R., Day, D. A., Froyd, K. D., Heinold, B., Jo, D. S., Katich, J. M., Kodros, J. K., Nault, B. A., Pierce, J. R., Ray, E., Schacht, J., Schill, G. P., Schroder, J. C., Schwarz, J. P., Sueper, D. T., Tegen, I., Tilmes, S., Tsigaridis, K., Yu, P. and Jimenez, J. L.: Characterization of organic

aerosol across the global remote troposphere: a comparison of ATom measurements and global chemistry models, Atmos. Chem. Phys., 20(8), 4607–4635, 2020.

655 Hu, K., Lu, R., Wang, D.: Seasonal climatology of cut-off lows and associated precipitation patterns over Northeast China, Meteorol. Atmos. Phys., 106:37–48, https://doi.org/10.1007/s00703-009-0049-0, 2010.

Jimenez, J. L., Campuzano-Jost, P., Day, D. A., Nault, B. A., Price, D. J. and Schroder, J. C.: ATom: L2 Measurements from CU High-Resolution Aerosol Mass Spectrometer (HR-AMS), , doi:10.3334/ORNLDAAC/1716, 2019.

Jiménez, R., Herndon, S., Shorter, J. H., Nelson, D. D., McManus, J. B., and Zahniser, M. S.: Atmospheric trace gas
660 measurements using a dual quantum-cascade laser mid-infrared absorption spectrometer, Proc. SPIE, 5738, 318–331, https://doi.org/10.1117/12.597130, 2005.

Jiménez, R., Park, S., Daube, B. C., McManus, J. B., Nelson, D. D., Zahniser, M. S., and Wofsy, S. C.: A new quantum-cascade laser-based spectrometer for high-precision airborne CO_2 measurements, 13th WMO/IAEA Meeting of Experts on Carbon Dioxide Concentration and Related Tracers Measurement Techniques, WMO/TD-No. 1359;
665 GAW Report- No. 168, 100–105, 2006.

Kort, E. A., Eluszkiewicz, J., Stephens, B. B., Miller, J. B., Gerbig, C., Nehrkorn, T., Daube, B. C., Kaplan, J. O., Houweling, S., and Wofsy, S. C.: Emissions of CH_4 and N_2O over the United States and Canada based on a receptor-oriented modeling framework and COBRA-NA atmospheric observations, Geophs. Res. Letters, vol. 35, L18808, doi:10.1029/2008GL034031, 2008.

670 Kort, E. A., Andrews, A. E., Dlugokencky, E., Sweeney, C., Hirsch, A., Eluszkiewicz, J., Nehrkorn, T., Michalak, A., Stephens, B., Gerbig, C., Miller, J. B., Kaplan, J., Houweling, S., Daube, B. C., Tans, P. and Wofsy, S. C.: Atmospheric constraints on 2004 emissions of methane and nitrous oxide in North America from atmospheric measurements and a receptor-oriented modeling framework, J. Integr. Environ. Sci., 7:S1, 125-133, https://doi.org/ 10.1080/19438151003767483, 2010.

675 Kort, E. A., Patra, P. K., Ishijima, K., Daube, B. C., Jiménez, R., Elkins, J., Hurst, D., Moore, F. L., Sweeney, C. and Wofsy, S. C.: Tropospheric distribution and variability of N_2O: Evidence for strong tropical emissions, Geophys. Res. Lett., 38, L15806, https://doi.org/10.1029/2011GL047612, 2011.

Krause, J., Hoor, P., Engel, A., Plöger, F., Grooß, J.-U., Bönisch, H., Keber, T., Sinnhuber, B.-M., Woiwode, W. and Oelhaf, H.: Mixing and ageing in the polar lower stratosphere in winter 2015–2016, Atmos. Chem. Phys., 18,
680 6057–6073, https://doi.org/10.5194/acp-18-6057-2018, 2018.

Lin, J. C., Gerbig, C., Wofsy, S. C., Andrews, A. E., Daube, B. C., Davis, K. J. and Grainger, C. A.: A near-field tool for simulating the upstream influence of atmospheric observations: The Stochastic Time- Inverted Lagrangian Transport (STILT) model, J. Geophys. Res. Atmos., 108(D16), 4493, https://doi.org/10.1029/2002JD003161, 2003.

685 Liu, Y., Yvon-Lewis, S. A., Thornton, D. C. O., Butler, J. H., Bianchi, T. S., Campbell, L., Hu, L. and Smith, R. W.: Spatial and temporal distributions of bromoform and dibromomethane in the Atlantic Ocean and their relationship with photosynthetic biomass, J. Geophys. Res. Oceans, vol. 118, 3950–3965, https://doi.org/10.1002/jgrc.20299, 2013.

Lueker, T. J., Keeling, R. F. and Dubey, M. K.: The oxygen to Carbon Dioxide Ratios observed in Emissions from a
690 Wildfire in the Northern California, Geophysical Research Letters, vol. 28, no. 12, pages 2413-2416, doi: 10.1029/2000GL011860, 2001.

Lueker, T. J., Walker, S. J., Vollmer, M. K., Keeling, R. F., Nevison, C. D., Weiss, R. F. and Garcia, H. E.: Coastal upwelling air-sea fluxes revealed in atmospheric observations of O_2/N_2, CO_2 and N_2O, Geophys. Res. Lett., vol. 30, no. 6, 1292, https://doi.org/10.1029/2002GL016615, 2003.

695 Lueker, T. J.: Coastal upwelling fluxes of O_2, N_2O, and CO_2 assessed from continuous atmospheric observations at Trinidad, California, Biogeosciences, 1, 101–111, https://doi.org/10.5194/bg-1-101-2004, 2004.

Montzka, S., Moore, F. and Sweeney, C.: ATom: L2 Measurements from the Programmable Flask Package (PFP) Whole Air Sampler, ORNL DAAC, doi:10.3334/ORNLDAAC/1746, 2019.

Moore, F., Dutton, G., Elkins, J. W., Hall, B., Hurst, D., Nance, J. D., and Thompson, T: PANTHER Data from SOLVE-
700 II Through CR-AVE: A Contrast Between Long- and Short-Lived Compounds, American Geophysical Union, Fall Meeting 2006, abstract #A41A-0025, 2006.

Nevison, C. D., Dlugokencky, E., Dutton, G., Elkins, J. W., Fraser, P., Hall, B., Krummel, P. B., Langenfelds, R. L., O'Doherty, S, Prinn, R. G., Steele, L. P., and Weiss, R. F.: Exploring causes of interannual variability in the seasonal cycles of tropospheric nitrous oxide, Atmos. Chem. Phys., 11, 3713–3730, https://doi.org/10.5194/acp-11-3713-2011, 2011.

705

Nevison, C.D., Keeling, R. F., Weiss, R. F., Popp, B. N., Jin, X., Fraser, P. J., Porter, L. W., and Hess, P. G.: Southern Ocean ventilation inferred from seasonal cycles of atmospheric N₂O and O₂/N₂ at Cape Grim, Tasmania, Tellus, 57B, 218–229, 2005.

Nevison, C.D., Weiss, R. F. and Erickson III, D. J.: Global oceanic emissions of nitrous oxide, J. Geophys. Res. Oceans, 100, C8, 5809-15820, https://doi.org/10.1029/95JC00684, 1995.

710

Pires M. and Rossi, M. J.: The Heterogeneous Formation of N₂O in the Presence of Acidic Solutions: Experiments and Modeling, International Journal of Chemical Kinetics, Vol. 29, 869–891, 1997.

Randerson, J. T., van der Werf, G. R., Giglio, L., Collatz, G. J. and Kasibhatla, P. S.: Global Fire Emissions Database, Version 4.1 (GFEDv4). ORNL DAAC, Oak Ridge, Tennessee, USA, https://doi.org/10.3334/ORNLDAAC/1293, 2018

715

Ravishankara, A. R., Daniel, J. S. and Portmann, R. W.: Nitrous oxide (N₂O): the dominant ozone-depleting substance emitted in the 21st century., Science, 326(5949), 123–5, https://doi.org/10.1126/science.1176985, 2009.

Rothman, L.S., Jacquemart, D., Barbe, A., Benner, D. C., Birk, M., Brown, L.R., Carleer, M.R., Chackerian Jr., C., Chance, K., Couderth, L.H., Dana, V., Devi, V.M., Flaud, J.-M., Gamache, R.R., Goldman, A., Hartmann, J.-M., Jucks, K.W., Maki, A.G., Mandin, J.-Y., Massie, S.T., Orphal, J., Perrin, A., Rinsland, C.P., Smith, M.A.H., Tennyson, J., Tolchenov, R.N., Toth, R.A., Vander Auwera, J., Varanasi, P., Wagner, G.: The HITRAN 2004 molecular spectroscopic database, Journal of Quantitative Spectroscopy & Radiative Transfer 96, 139–204, 2005.

720

Ryerson, T. B., Thompson, C., Peischl, J. and Bourgeois, I.: ATom: L2 In Situ Measurements from NOAA Nitrogen Oxides and Ozone (NOyO3) Instrument, ORNL DAAC, 2019, https://doi.org/10.3334/ORNLDAAC/1734, 2019.

725

Saikawa, E., Prinn, R. G., Dlugokencky, E., Ishijima, K., Dutton, G. S. , Hall, B. D., Langenfelds, R., Tohjima, Y., Machida, T., Manizza, M., Rigby, M. , O'Doherty, S., Patra, P. K., Harth, C. M., Weiss, R. F., Krummel, P. B., van der Schoot, M., Fraser, P. J., Steele, L. P., Aoki, S., Nakazawa, T., and Elkins, J. W. : Global and regional emissions estimates for N₂O, Atmos. Chem. Phys., 14, 4617–4641, https://doi.org/10.5194/acp-14-4617-2014, 2014.

730

Santoni, G. W., Daube, B. C., Kort, E. A., Jiménez, R., Park, S., Pittman, J. V., Gottlieb, E., Xiang, B., Zahniser, M. S., Nelson, D. D., McManus, J. B., Peischl, J., Ryerson, T. B., Holloway, J. S., Andrews, A. E., Sweeney, C., Hall, B., Hintsa, E. J., Moore, F. L., Elkins, J. W., Hurst, D. F., Stephens, B. B., Bent, J., and Wofsy, S. C.: Evaluation of the airborne quantum cascade laser spectrometer (QCLS) measurements of the carbon and greenhouse gas suite – CO₂, CH₄, N₂O, and CO – during the CalNex and HIPPO campaigns, Atmos. Meas. Tech., 7, 1509-1526, https://doi.org/10.5194/amt-7-1509-2014, 2014.

735

St. Clair, J.M., McCabe, D. C., Crounse, J. D., Steiner, U. and Wennberg, P. O.: Chemical ionization tandem mass spectrometer for the *in situ* measurement of methyl hydrogen peroxide, Rev. Sci. Instrum., 81, 094102, https://doi.org/10.1063/1.3480552, 2010.

Stephens, B. B., Keeling, R. F., Heimann, M., Six, K. D., Murnane, R. and Caldeira, K.: Testing global ocean carbon cycle models using measurements of atmospheric O₂ and CO₂ concentration, Global Biochemical cycles, vol. 12, no. 12, pages 213-230, 1998.

740

Syakila, A. and Kroeze, C.: The global nitrous oxide budget revisited, Greenhouse Gas Measurement and Management, 1:1, 17-26, https://doi.org/10.3763/ghgmm.2010.0007, 2011.

Thompson, R. L., Ishijima, K., Saikawa, E., Corazza, M., Karstens, U., Patra, P. K., Bergamaschi, P., Chevallier, F., Dlugokencky, E., Prinn, R. G., Weiss, R. F., O'Doherty, S., Fraser, P. J., Steele, L. P., Krummel, Vermeulen, A., Tohjima, Y., Jordan, A., Haszpra, L., Steinbacher, M., Van der Laan, S., Aalto, T., Meinhardt, F., Popa, M. E., Moncrieff, J., and Bousquet, P.: TransCom N₂O model inter-comparison – Part 2: Atmospheric inversion estimates of N₂O emissions, Atmos. Chem. Phys., 14, 6177–6194, https://doi.org/10.5194/acp-14-6177-2014, 2014b.

745

Thompson, R. L., Patra, P. K., Ishijima, K., Saikawa, E., Corazza, M., Karstens, U., Wilson, C., Bergamaschi, P., Dlugokencky, E., Sweeney, C., Prinn, R. G., Weiss, R. F., O'Doherty, S., Fraser, P. J., Steele, L. P., Krummel, P. B., Saunois, M., Chipperfield, M., and Bousquet, P.: TransCom N₂O model inter-comparison – Part 1: Assessing

750

the influence of transport and surface fluxes on tropospheric N$_2$O variability, Atmos. Chem. Phys., 14, 4349–4368, https://doi.org/10.5194/acp-14-4349-2014, 2014a.

Tian, H., Lu, C., Chen G., Tao, B., Pan, S., Del Grosso, S. J., Xu, X., Bruhwiler, L., Wofsy, S.C., Kort, E. A. and Prior, S. A.: Contemporary and projected biogenic fluxes of methane and nitrous oxide in North American terrestrial ecosystems, Front Ecol Environ 2012; 10(10): 528–536, https://doi.org/10.1890/120057, 2012.

Tian, H., Xu, R., Canadell, J.G. et al.: A comprehensive quantification of global nitrous oxide sources and sinks, Nature, 586, 248–256, https://doi.org/10.1038/s41586-020-2780-0, 2020.

Upstill-Goddard, R. C., Salter, M. E., Mann, P. J., Barnes, J., Poulsen, J., Dinga, B., Fiske, G. J., and Holmes, R. M.: The riverine source of tropospheric CH$_4$ and N$_2$O from the Republic of Congo, Western Congo Basin, Biogeosciences, 14, 2267–2281, https://doi.org/10.5194/bg-14-2267-2017, 2017.

Wang, J., Li, J., Ye, J. et al: Fast sulfate formation from oxidation of SO$_2$ by NO$_2$ and HONO observed in Beijing haze. Nat. Commun., 11, 2844, https://doi.org/10.1038/s41467-020-16683-x, 2020.

WMO: WMO Greenhouse Gas Bulletin., 2018.

Wofsy, S. C., Afshar, S., Allen, H. M., Apel, E., Asher, E. C., Barletta, B., Bent, J., Bian, H., Biggs, B. C., Blake, D. R., Blake, N., Bourgeois, I., Brock, C. A., Brune, W. H., Budney, J. W., Bui, T. P., Butler, A., Campuzano-Jost, P., Chang, C. S., Chin, M., Commane, R., Correa, G., Crounse, J. D., Cullis, P. D., Daube, B. C., Day, D. A., Dean-Day, J. M., Dibb, J. E., DiGangi, J. P., Diskin, G. S., Dollner, M., Elkins, J. W., Erdesz, F., Fiore, A. M., Flynn, C. M., Froyd, K., Gesler, D. W., Hall, S. R., Hanisco, T. F., Hannun, R. A., Hills, A. J., Hintsa, E. J., Hoffman, A., Hornbrook, R. S., Huey, L. G., Hughes, S., Jimenez, J. L., Johnson, B. J., Katich, J. M., Keeling, R. F., Kim, M. J., Kupc, A., Lait, L. R., Lamarque, J.-F., Liu, J., McKain, K., Mclaughlin, R. J., Meinardi, S., Miller, D. O., Montzka, S. A., Moore, F. L., Morgan, E. J., Murphy, D. M., Murray, L. T., Nault, B. A., Neuman, J. A., Newman, P. A., Nicely, J. M., Pan, X., Paplawsky, W., Peischl, J., Prather, M. J., Price, D. J., Ray, E., Reeves, J. M., Richardson, M., Rollins, A. W., Rosenlof, K. H., Ryerson, T. B., Scheuer, E., Schill, G. P., Schroder, J. C., Schwarz, J. P., St. Clair, J. M., Steenrod, S. D., Stephens, B. B., Strode, S. A., Sweeney, C., Tanner, D., Teng, A. P., Thames, A. B., Thompson, C. R., Ullmann, K., Veres, P. R., Vieznor, N., Wagner, N. L., Watt, A., Weber, R., Weinzierl, B., Wennberg, P., Williamson, C. J., Wilson, J. C., Wolfe, G. M., Woods, C. T., and Zeng, L. H.: ATom: Merged Atmospheric Chemistry, Trace Gases, and Aerosols, ORNL DAAC, Oak Ridge, Tennessee, USA, https://doi.org/10.3334/ORNLDAAC/1581, 2018.

Wofsy, S. C., the HIPPO Science Team, and Cooperating Modelers and Satellite Teams: HIAPER Pole-to-Pole Observations (HIPPO): Fine grained, global scale measurements for determining rates for transport, surface emissions, and removal of climatically important atmospheric gases and aerosols, Philos. T. Roy. Soc. A, 369, 2073–2086, https://doi.org/10.1098/rsta.2010.0313, 2011.

Xiang, B., Miller, S. M., Kort, E. A., Santoni, G. W., Daube, B. C., Commane, R., Angevine, W. M., Ryerson, T. B. , Trainer, M. K. , Andrews, A. E., Nehrkorn, T., Tian, H., and Wofsy, S. C.: Nitrous oxide (N$_2$O) emissions from California based on 2010 CalNex airborne measurements, J. Geophys. Res. Atmos., 118, 2809–2820, https://doi.org/10.1002/jgrd.50189, 2013.

Yang, Simon, Chang, B. X., Warner, M. J., Weber, T. S., Bourbonnais, A. M., Santoro, A. E., Kock, A., Sonnerup, R. E., Bullister, J. L. Wilson, S. T. and Bianchi, D.: Global reconstruction reduces the uncertainty of oceanic nitrous oxide emissions and reveals a vigorous seasonal cycle, P. Natl. Acad. Sci. USA, 117 (22), 11954-11960; https://doi.org/10.1073/pnas.1921914117, 2020.

795
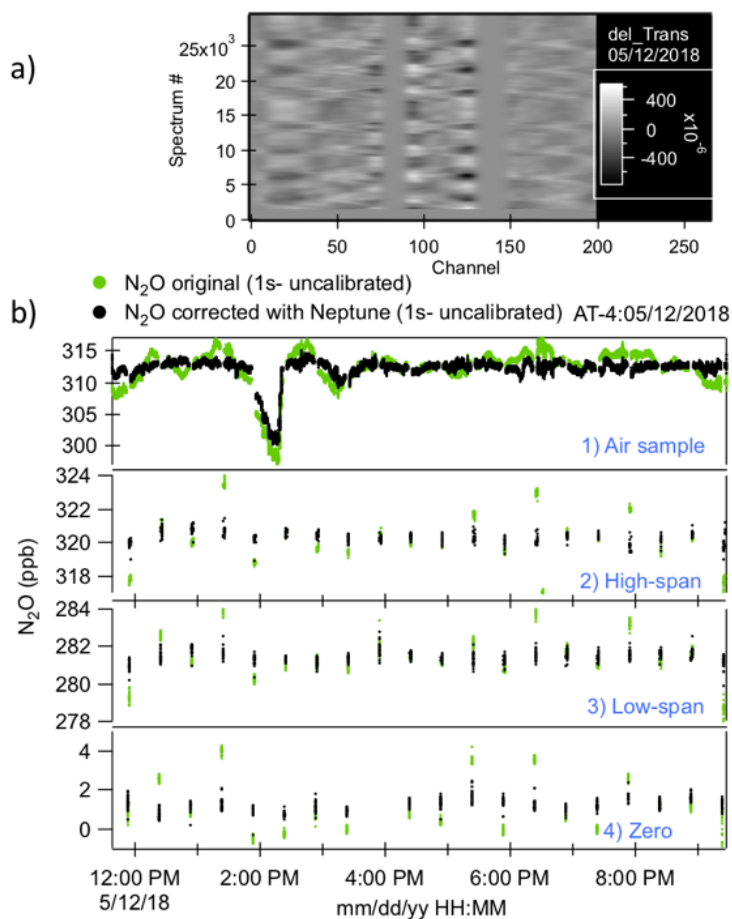
Figure 1: (a) A processed spectral array from the ATom-4 flight on 12 May 2018. "Channel" represents a point number in the spectra. Spectra have been grouped by type (i.e., calibration, ambient), with averages subtracted, absorption lines zeroed out (near channels 75, 140, and 225), and smoothed to close to the linewidth. Shifts in fringe phases during altitude changes are apparent. (b) Time series of ambient air samples, high-span, low-span, and zeros for the same flight as (a). Green dots are the original N₂O data record. Black dots are the N₂O data corrected with Neptune (no calibration applied at this point).

800
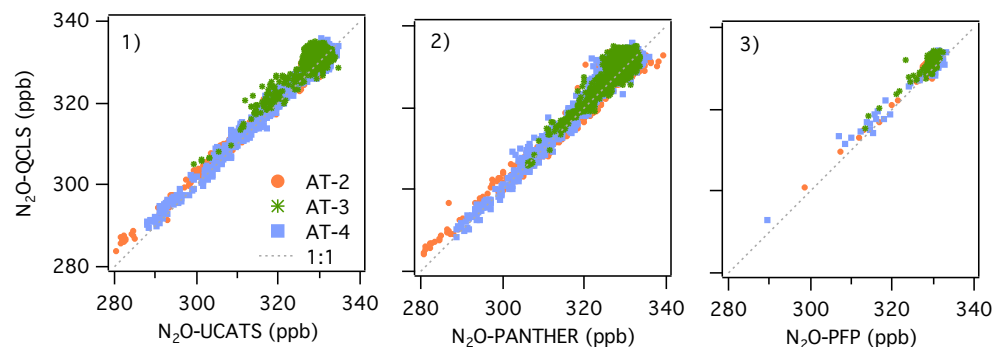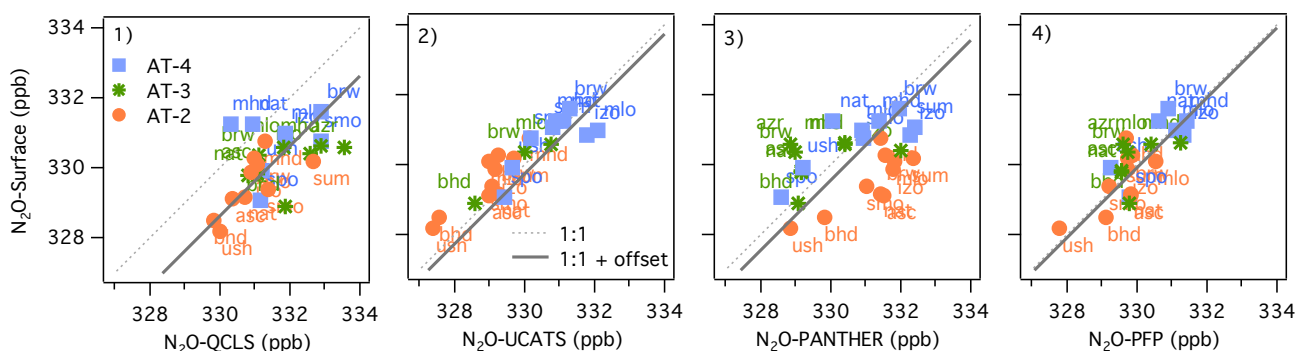
Figure 2: (a) Comparisons between Neptune-corrected QCLS N₂O and (1) UCATS N₂O, (2) PANTHER N₂O, and (3) PFP N₂O for ATom-2 (orange circles), ATom-3 (green stars), and -4 (blue squares). We used the 10s averaged merged file to compare QCLS, UCATS and PANTHER data. PFP instrument has a longer sampling time (30s to few minutes). The 1:1 line is shown as a dashed line. (b) B) Comparisons between NOAA N₂O surface flask measurements and Neptune-corrected and airborne data from (d) QCLS N₂O, (e) UCATS N₂O, (f) PANTHER N₂O, (g) and PFP N₂O for ATom-2, -3, and -4, similar to (a)–(c). The solid line shows the 1:1 relationship + offset. For (d)–(g) plots, the airborne data are the mean N₂O values within ± 5° latitude of each surface station and between 1 and 4 km.

815
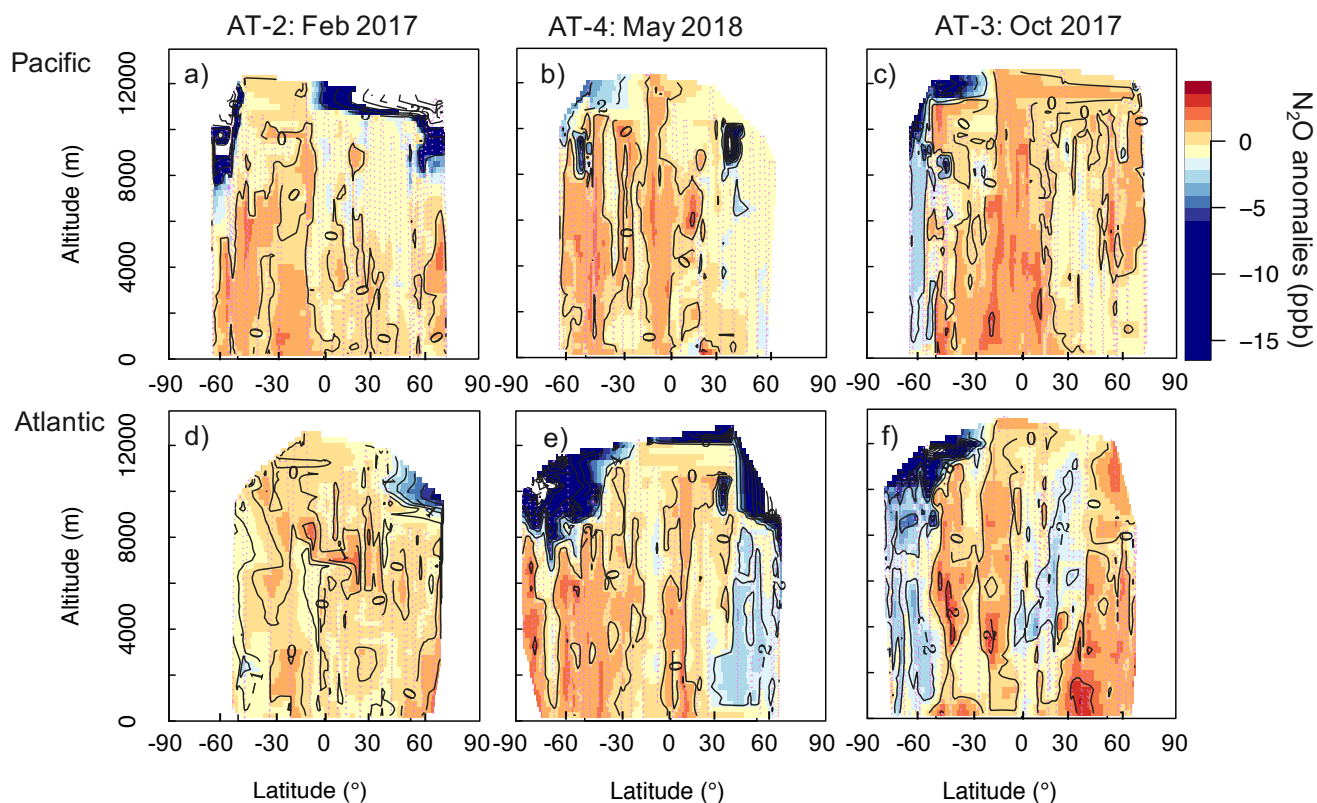
Figure 3: Cross-sections of N₂O anomalies (ppb), representing the differences between the airborne N₂O (10-s resolution) and the surface N₂O mixing ratios interpolated to 0.25° latitude and 250 m altitude for each deployment. Shown are the N₂O anomalies over (a)–(c) the Pacific and (d)–(f) the Atlantic, and each column represents a deployment (ordered by season, ATom-2, -4 and -3). The color-scale ranges from -15 to 5 ppb. Values between -50 and -15 ppb, observed at the highest
820 **altitudes (>10 km) are shown in white for a better visualization of small changes in positive anomalies. Lilac dashed lines represent the fight tracks. Black contours are areas of the N₂O anomalies.**

825
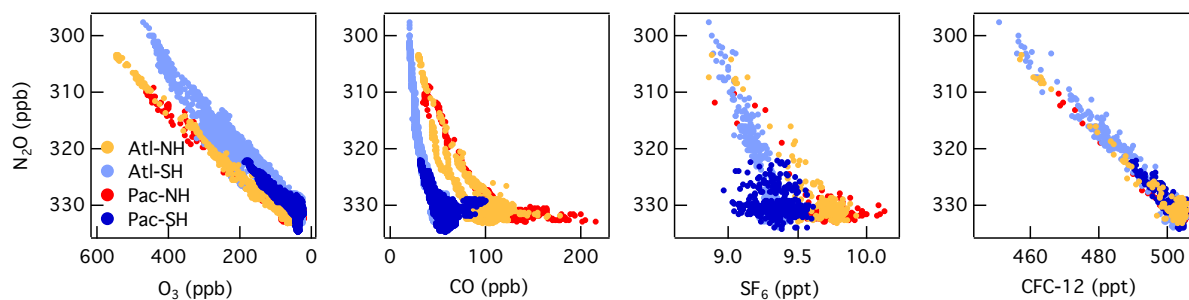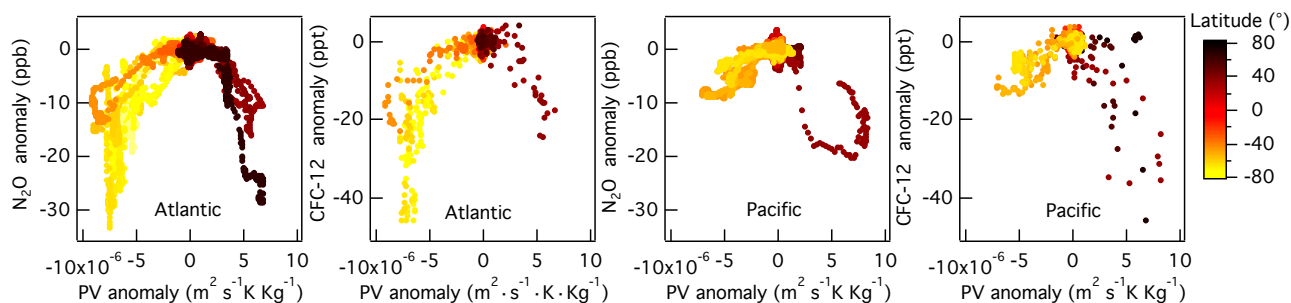
Figure 4: (a) Correlations between N₂O and (a) O₃, (b) CO, (c) SF₆, and (d) CFC-12 at mid and high latitudes (30°–85° N) during NH spring (ATom-4). The data are colored as a function of the ocean basin and hemisphere: Pacific North Mid-High Latitudes (Pac-NH, >30° N) in red, Pacific South Mid-High Latitudes (Pac-SH, <30° S) in dark blue, Atlantic South Mid-High Latitudes (Atl-SH, <30° S) in light blue and Atlantic North Mid-High Latitudes (Atl-NH, >30° N) in orange. Note that the N₂O and O₃ axes are reversed. **(b)** Correlations between anomalies in potential vorticity relative to its mean latitudinal distribution in the free troposphere (2–8 km) and anomalies in N₂O and CFC-12 as a function of latitude during spring (ATom-4) over the Pacific and Atlantic basins. Mid-latitudes are shown in orange in the SH and clear brown in the NH.
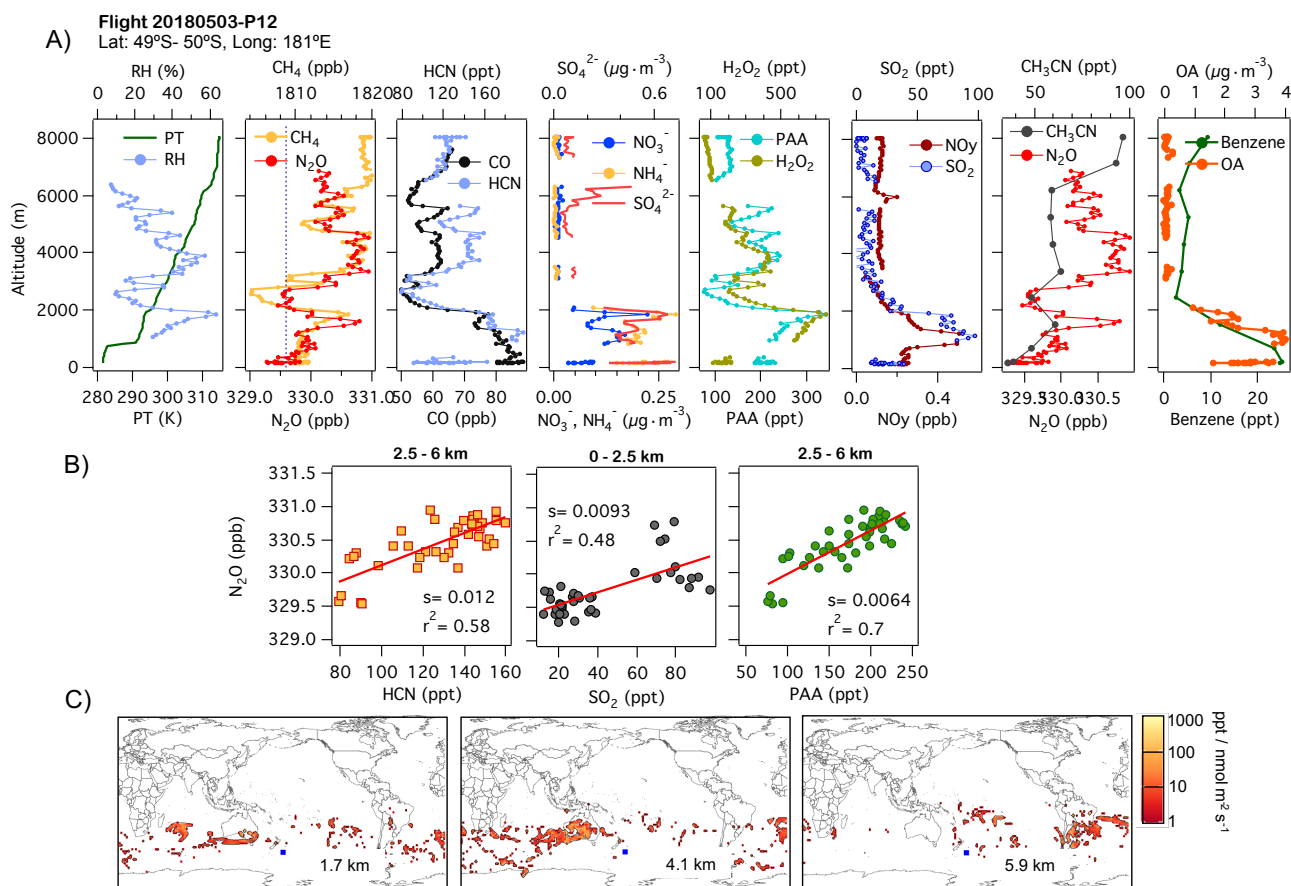
Figure 5: (a) Vertical profiles of Potential Temperature (PT), Relative Humidity (RH), N_2O, CH_4, CO, HCN, NO_3^-, NH_4^+, SO_4^{2+}, H_2O_2, PAA ($CH_3C(O)OOH$), SO_2, NO_y, CH_3CN, benzene and organic aerosols (OA) from profile 12 on 3 May 2018. Dotted blue line in plot A2 represents the NOAA-MBL reference (N_2O-MBL) at the latitude of the flight. **(b)** Correlations between N_2O and HCN and PAA for altitudes between 2.5 and 6 km and between N_2O and SO_2 for altitudes between 0 and 2.5 km indicate an admixture of marine, biomass burning, urban sources, and oil and gas industry contributions to N_2O mixing ratios (s represents the slope of the linear fit). **(c)** Footprint maps tracing surface regions influencing mixing ratios measured at the altitude ranges of 1–2, 2.5–5 and 5–7 km, respectively. Blue squares show the sample locations. Values below 3 ppt / (nmol m^{-2} s^{-1}) are not included.

845
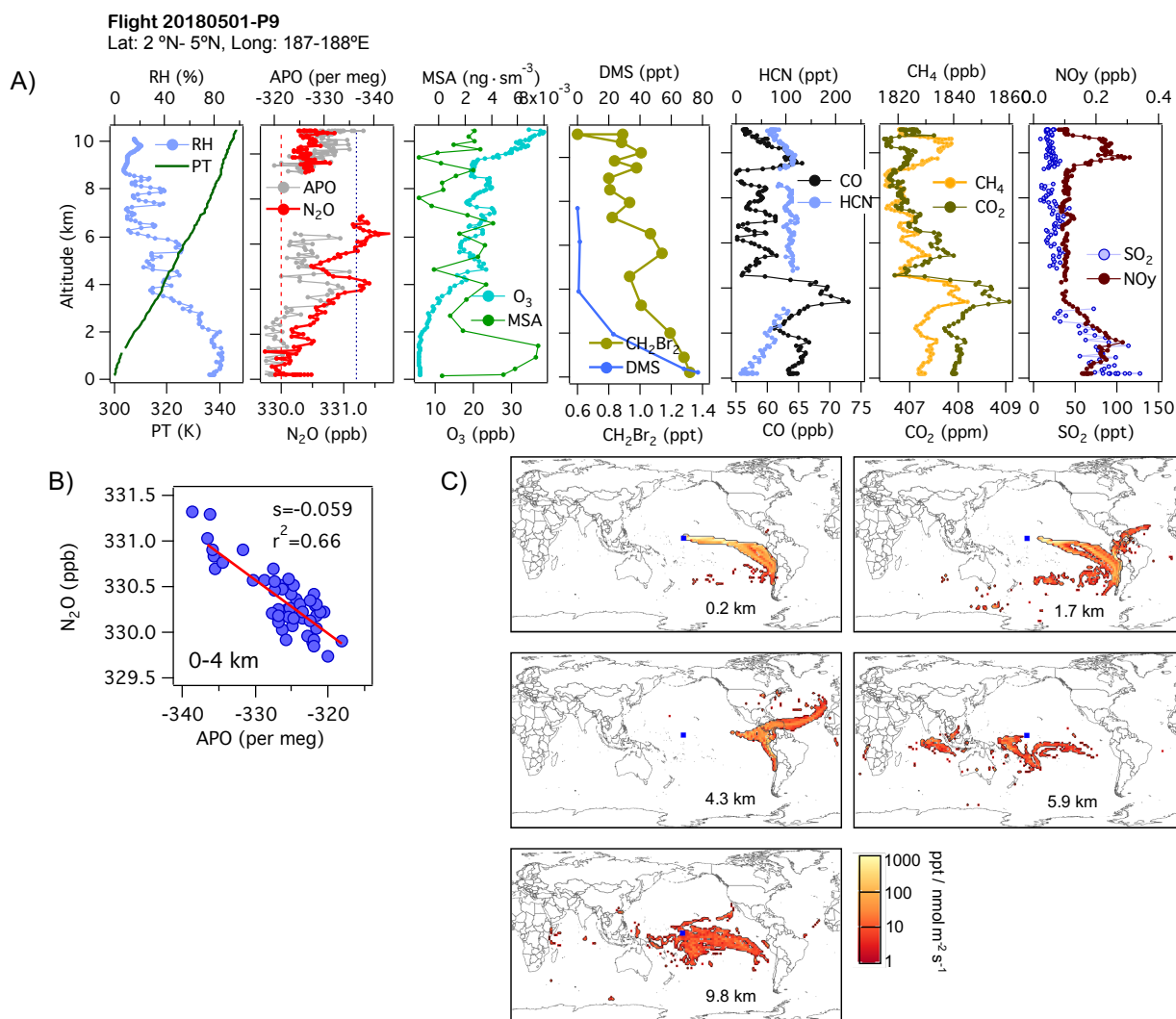
Figure 6: (a) Vertical profiles of PT and RH and tracers, N_2O, APO, O_3, MSA, CH_2Br_2, DMS, CO, HCN, CH_4, CO_2, SO_2 and NOy, corresponding to profile 9 on 1 May 2018. Dotted blue line in plot A2 represents the NOAA-MBL reference (N_2O-MBL) at the latitude of the flight. Dashed red line shows the N_2O-MBL at the origin of the airmasses suggested by the footprints (25°S). (b) N_2O - APO correlations between 0 and 4 km possibly describing the latitudinal gradient of N_2O (s represents the slope of the linear fit). (c) Footprint maps tracing surface regions influencing mixing ratios measured at the altitude ranges of 0–2, 2–4, 3–5, 5–7 and 9–11 km, respectively. Blue squares show the sample locations. Values below 3 ppt / $nmol^{-1}$ m^{-2} s^{-1} are not included. Note that the APO axes are reversed.

850

855
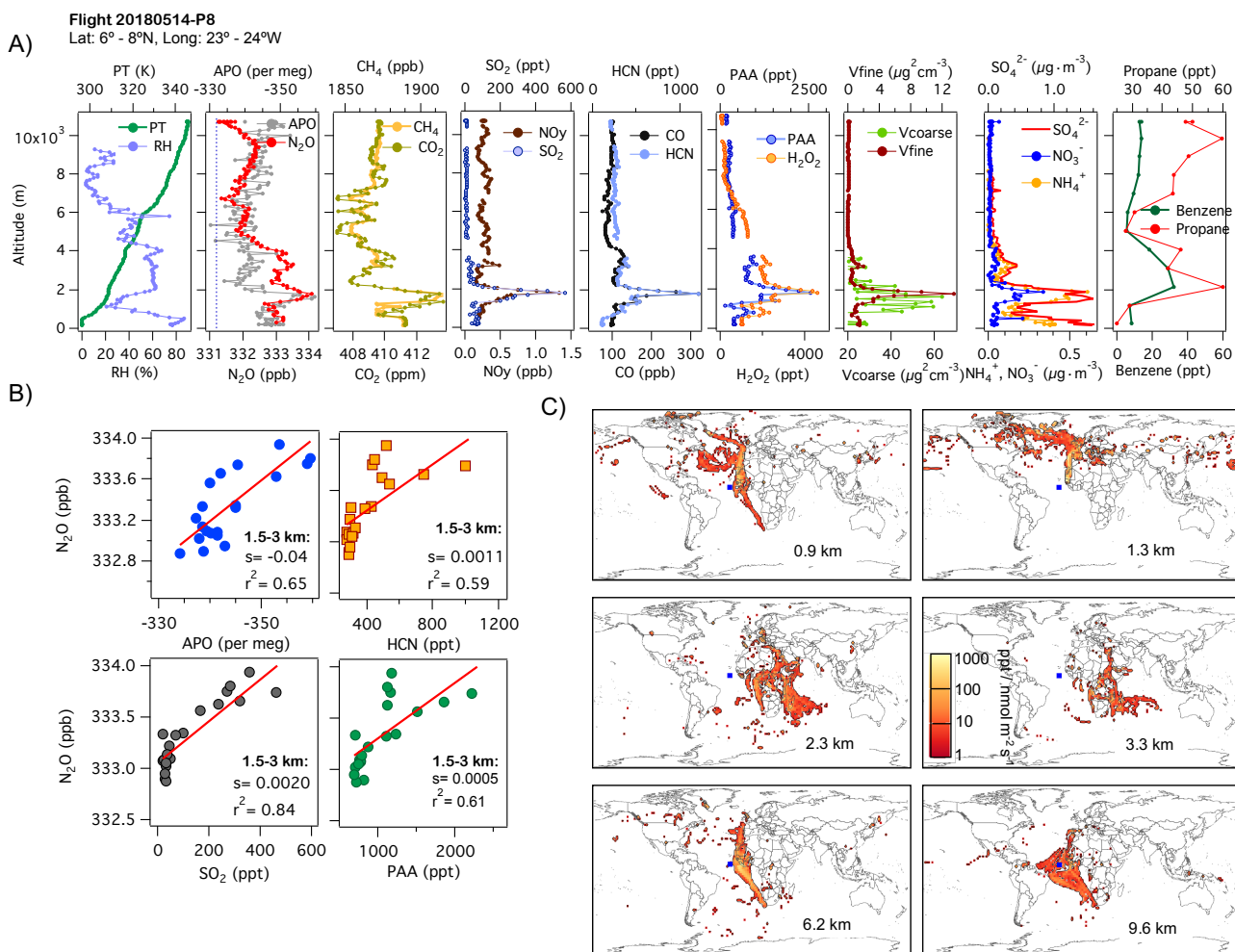
Figure 7: (a) Vertical profiles of PT, RH, and tracers, N_2O, APO, organic aerosol (OA), chloride, CO_2, CH_4, HCN, CO, SO_2, NOy, NO_3^-, NH_4^+, SO_4^{2+}, benzene and propane, corresponding to profile 8 on 14 May 2018. Dotted blue line in plot A2 represents the NOAA-MBL reference (N_2O-MBL) at the latitude of the flight. (b) Correlations between N_2O and APO, HCN, SO_2, and propane between 1 and 3 km show possible contributions from marine upwelling, biomass burning and oil and gas industry, supported by the footprints (s represents the slope of the linear fit). (c) Footprint maps tracing surface regions influencing mixing ratios measured at the altitude ranges of 0–1, 2–4, 4–5, 5–7 and 7–10 km, respectively. Blue square shows the sample point. Values below 3 ppt / nmol m^{-2} s^{-1} are not included. Note that the APO axes are reversed.

860
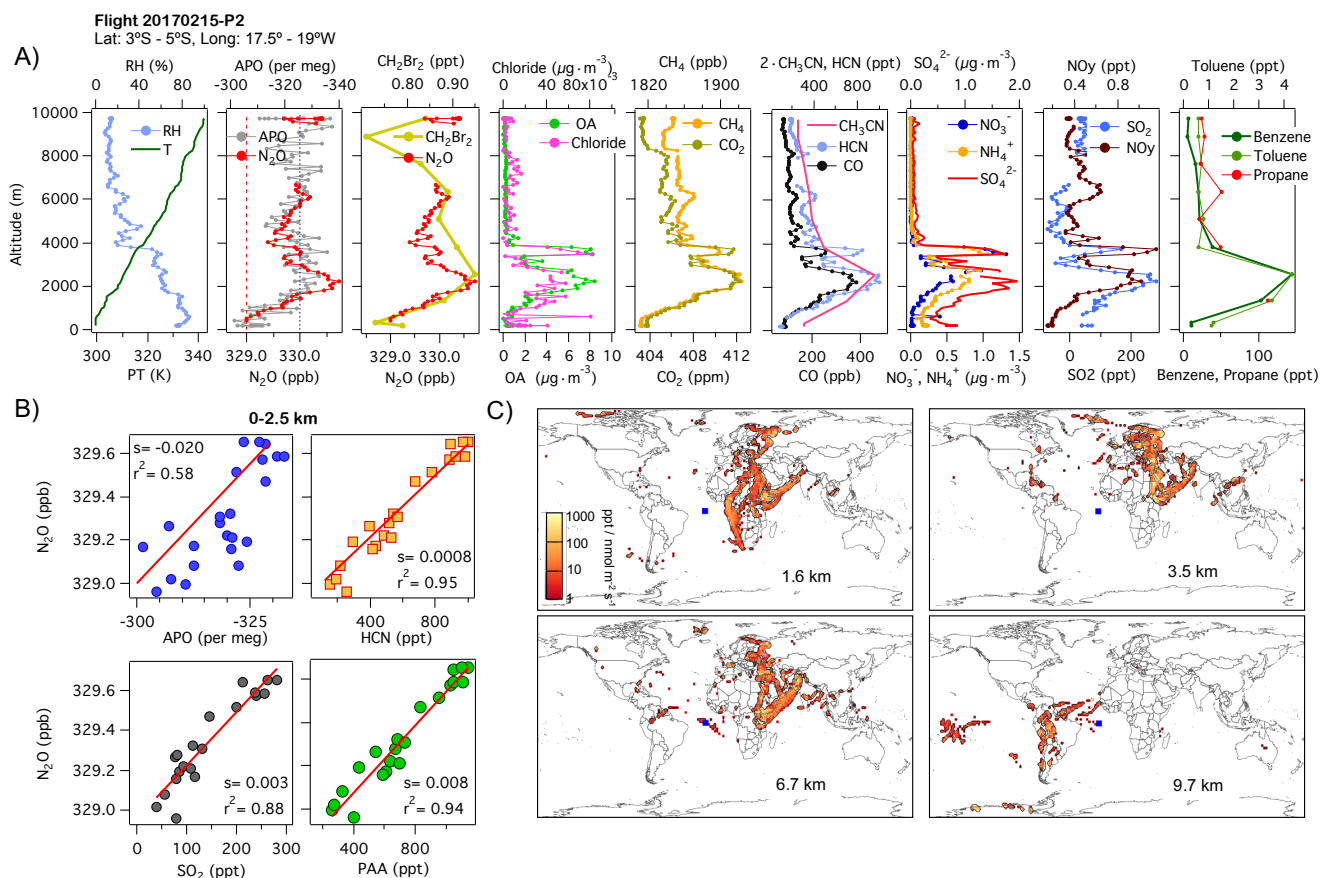
865 **Figure 8: (a) Vertical profiles of PT, RH, and tracers, N_2O, APO, CH_2Br_2, organic aerosol (OA), non-refractory chloride, CO_2, CH_4, HCN, CO, CH_3CN, NO_3^-, NH_4^+, SO_4^{2+}, SO_2, NOy, benzene and propane, corresponding to profile 2 on 15 February 2017. Dotted blue line in plot A2 represents the NOAA-MBL reference (N_2O-MBL) at the latitude of the flight, and red dashed line shows the NOAA-MBL at the origin of the southern airmasses shown by the footprints below 2 km (20°S). (b) Correlations between N_2O and APO, HCN and SO_2, for data observed below 2.5 km, indicate an admixture of marine,**
870 **biomass burning, urban sources, and oil and gas industry contributions to N_2O mixing ratios (s represents the slope of the linear fit). (c) Footprint maps tracing surface regions influencing mixing ratios measured at the altitude ranges of 0–2, 2–3, 3–4 and 4–7 km, respectively. Blue squares show the sample point. Values below 3 ppt / nmol m^{-2} s^{-1} are not included in the footprint plot. Note that APO axes are reversed.**

875
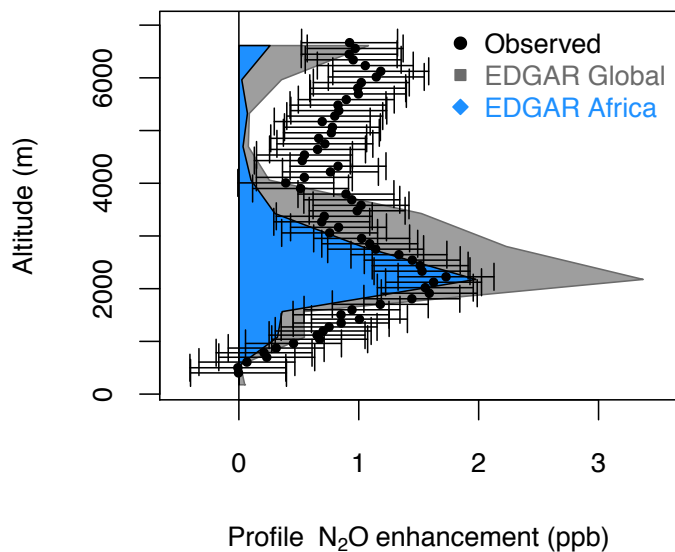
Figure 9. N₂O enhancements estimated by EDGAR for the globe (grey polygons) and for the African region (blue polygons) and the observed QCLS-N₂O enhancement relative to the NOAA-MBL N₂O reference at the origin of the southern airmasses shown by the footprints below 2 km for the profile 2017/02/15-P2 (20°S, 329 ppb).

880